https://doi.org/10.5194/gmd-2020-284
Preprint. Discussion started: 26 October 2020

Geoscientific Model Development
Discussions
Open Access

BCC-CSM2-HR: A High-Resolution Version of the Beijing Climate Center Climate System Model

Tongwen Wu[1*], Rucong Yu[1], Yixiong Lu[1], Weihua Jie[1], Yongjie Fang[1], Jie Zhang[1], Li Zhang[1], Xiaoge Xin[1], Laurent Li[1,2], Zaizhi Wang[1], Yiming Liu[1], Fang Zhang[1], Fanghua Wu[1], Min Chu[1], Jianglong Li[1], Weiping Li[1], Yanwu Zhang[1], Xueli Shi[1], Wenyan Zhou[1], Junchen Yao[1], Xiangwen Liu[1], He Zhao[1], Jinghui Yan[1], Min Wei[3], Wei Xue[4], Anning Huang[5], Yaocun Zhang[5], Yu Zhang[6], Qi Shu[7]

1. *Beijing Climate Center, China Meteorological Administration, Beijing, China*
2. *Laboratoire de Météorologie Dynamique, IPSL, CNRS, Sorbonne Université, Ecole Normale Supérieure, Ecole Polytechnique, Paris 75005, France*
3. *National Meteorological Information Center, China Meteorological Administration, Beijing 100081, China.*
4. *Tsinghua University, Beijing 100084, China*
5. *Nanjing University, Nanjing 210023, China*
6. *Chengdu University of Information Technology, Chengdu 610225, China*
7. *The First Institute of Oceanography of the Ministry of Natural Resources, Qingdao 266061, China*

*Corresponding author: Tongwen Wu (twwu@cma.gov.cn)

https://doi.org/10.5194/gmd-2020-284
Preprint. Discussion started: 26 October 2020

Abstract

BCC-CSM2-HR is a high-resolution version of the Beijing Climate Center (BCC) Climate System Model. Its development is on the basis of the medium-resolution version BCC-CSM2-MR which is the baseline for BCC participation to the Coupled Model Intercomparison Project Phase 6 (CMIP6). This study documents the high-resolution model, highlights major improvements in the representation of atmospheric dynamic core and physical processes. BCC-CSM2-HR is evaluated for present-day climate simulations from 1971 to 2000, which are performed under CMIP6-prescribed historical forcing, in comparison with its previous medium-resolution version BCC-CSM2-MR. We focus on basic atmospheric mean states over the globe and variabilities in the tropics including the tropic cyclones (TCs), the El Niño–Southern Oscillation (ENSO), the Madden-Julian Oscillation (MJO), and the quasi-biennial oscillation (QBO) in the stratosphere. It is shown that BCC-CSM2-HR keeps well the global energy balance and can realistically reproduce main patterns of atmosphere temperature and wind, precipitation, land surface air temperature and sea surface temperature. It also improves in the spatial patterns of sea ice and associated seasonal variations in both hemispheres. The bias of double intertropical convergence zone (ITCZ), obvious in BCC-CSM2-MR, is almost disappeared in BCC-CSM2-HR. TC activity in the tropics is increased with resolution enhanced. The cycle of ENSO, the eastward propagative feature and convection intensity of MJO, the downward propagation of QBO in BCC-CSM2-HR are all in a better agreement with observation than their counterparts in BCC-CSM2-MR. We also note some weakness in BCC-CSM2-HR, such as the excessive cloudiness in the eastern basin of the tropical Pacific with cold Sea Surface Temperature (SST) biases and the insufficient number of tropical cyclones in the North Atlantic.

https://doi.org/10.5194/gmd-2020-284
Preprint. Discussion started: 26 October 2020

1. Introduction.

Accurately modeling climate and weather is a major challenge for the scientific community and needs high spatial resolution. However, many climate models, such as those involved in the Fifth Assessment Report on Climate Change (IPCC AR5), still use a spatial resolution of hundreds of kilometers (Flato et al., 2013). This nominal resolution is suitable for global-scale applications that run simulations for centuries into the future, but fails to capture small-scale phenomena and features that influence local or regional weather and climate events. This resolution is fine enough to simulate mid-latitude weather systems which evolve in thousands of kilometers, but insufficient to describe convective cloud systems that rarely extend beyond a few tens of kilometers. The study of Strachan et al. (2013) showed that while the average tropical cyclone number can be well simulated at a resolution of around 130 km, but grids finer than 60 km are needed to properly simulate the inter-annual variability of cyclone counts. Higher horizontal resolutions (i.e., 50 km) can further improve the simulated climatology of tropical cyclones (e.g., Oouchi et al., 2006; Zhao et al., 2009; Murakami et al., 2012; Manganello et al., 2012; Bacmeister et al., 2014; Wehner et al., 2015; Reed et al., 2015; Zarzycki et al., 2016). Growing evidence showed that high-resolution models (50 km or finer in the atmosphere) can reproduce the observed intensity of extreme precipitation (Wehner et al., 2010; Endo et al., 2012; Sakamoto et al., 2012). Some phenomena are sensitive to increasing resolution such as ocean mixing (Small et al., 2015), diurnal cycle of precipitation (Sato et al., 2009; Birch et al., 2014; Vellinga et al., 2016), QBO (Hertwig et al., 2015), the MJO's representation (Peatman et al., 2015), and monsoons (Sperber et al., 1994; Lal et al., 1997; Martin et al., 1999). Some small-scale processes such as mid-latitude storms and tropical cyclones, and ocean eddies also feedback on the simulated large-scale circulation, climate variability and extremes (Smith et al., 2000; Masumoto et al., 2004; Mizuta et al., 2006; Shaffrey et al., 2009; Masson et al., 2012; Doi et al., 2012; Rackow et al., 2016). Many studies (e.g. Ohfuchi et al., 2004; Zhao et al., 2009; Walsh et al., 2012; Bell et al., 2013; Strachan et al., 2013; Kinter et al. 2013; Demory et al., 2014; Schiemann et al., 2014; Small et al. 2014; Shaevitz et al., 2014; Hertwig et al., 2015;

https://doi.org/10.5194/gmd-2020-284
Preprint. Discussion started: 26 October 2020

Geoscientific Model Development Discussions
Open Access

Murakami et al., 2015; Hertwig et al., 2015; Roberts et al. 2016; Hewitt et al. 2016; Roberts C.D. et al, 2018; Roberts M.J. et al., 2019) show that enhanced horizontal resolution in atmospheric and ocean models has many beneficial impacts on model performance and helps to reduce model systematic biases.

High-resolution climate system modelling becomes a key activity within the climate research community, although increasing model resolution needs considerable computational resources. In 2004, the first high-resolution global climate model produced its first simulations within the Japanese Earth Simulator (Ohfuchi et al., 2004; Masumoto et al., 2004). At present day, performing high-resolution climate simulations for saying 50 km in the atmosphere and 0.25° in the ocean is still a very costly effort and can be realized only at a few research centers (e.g. Shaffrey et al., 2009; Delworth et al., 2012; Mizielinski et al., 2014; Bacmeister et al., 2014; Satoh et al., 2014; Roberts et al., 2018). A High Resolution Model Intercomparison Project (HighResMIP, Haarsma et al., 2016) is proposed as the primary activity within Phase 6 of the Coupled Model Intercomparison Project (CMIP6, Eyring et al., 2016) to investigate the impact of horizontal resolution on climate simulation fidelity and systematic model biases.

As a main climate modelling center in China (Wu et al., 2010, 2013, 2014, 2019, 2020; Xin et al., 2013, 2019; Li et al., 2019; Lu et al., 2020a,b), Beijing Climate Center (BCC), China Meteorological Administration, also put important efforts in developing high-resolution fully-coupled Beijing Climate Center Climate System Model (BCC-CSM-HR) (Yu et al., 2014). The currently released version (BCC-CSM2-HR, Table 1) is one of the three BCC model versions (Wu et al., 2019) involved in CMIP6 to run HighResMIP experiment. It is now in its pre-operational phase to become the next generation Beijing Climate Center Climate Prediction System to produce forecasts at leading times of two weeks to 1 year. The purpose of this paper is to evaluate its performance by comparing it with the previous version of medium resolution (BCC-CSM2-MR, Wu et al., 2019). In particular, we evaluate their performance to simulate large-scale mean climate and some important phenomena such as the ITCZ, tropical cyclones (TCs), MJO, and QBO which are

https://doi.org/10.5194/gmd-2020-284
Preprint. Discussion started: 26 October 2020

Geoscientific Model Development Discussions Open Access EGU

expected to be improved with enhanced resolution. A relevant description of BCC-CSM2-HR is shown in Section 2, and the experiment design is shown in Section 3. Main results of model performance are presented in Section 4.

2. Model description at high-resolution configuration

Due to the diversity of research and operational needs in BCC, a basic rule that we imposed to ourselves in the development of BCC-CSMs (Wu et al., 2019) is the construction of a traceable hierarchy of model versions running from a coarse grid (T42, approximately 280km), to a medium grid (T106, approximately 110×110 km), and to fine grid (T266, around 45×45 km). Actually, we fulfilled our target with an achievement to all of these model versions. All of them are fully-coupled models with four components, atmosphere, ocean, land surface and sea-ice, interacting with each other (Wu et al., 2013, 2019, 2020). They are physically coupled through fluxes of momentum, energy, water at their interfaces. The ocean - atmosphere coupling frequency is 30 minutes, which is sufficient to account for the diurnal cycle. As shown in Table 1, the medium resolution of BCC-CSM2-MR is at T106 for the atmosphere and has 46 layers with its model lid at 1.459 hPa. The resolution of the global ocean is of 1°lat.×1°lon. on average, but 1/3° lat.×1°lon. for the tropical oceans. BCC-CSM2-MR was described in detail in Wu et al. (2019). The atmosphere resolution of BCC-CSM2-HR is T266 on the globe and 56 layers with the top layer at 0.156 hPa (Figure 1) and model lid at 0.092 hPa (Table 1). The ocean and sea ice resolution in BCC-CSM2-HR is 1/4°lat.×1/4°lon. and 40 layers in depth. Compared to BCC-CSM2-MR, BCC-CSM2-HR is updated for its dynamical core and model physics in the atmospheric component (Table 1). The ocean and sea ice components are also updated from MOM4 and SIS4 (in BCC-CSM2-MR) to MOM5 and SIS5, respectively. The land component in the two versions of BCC-CSMs is BCC AVIM version 2 (Li et al., 2019).

2.1 Atmosphere Model

The atmospheric component of BCC-CSM2-MR is the medium resolution BCC-AGCM3-MR, with details being described in Wu et al. (2019) and in a series of

https://doi.org/10.5194/gmd-2020-284
Preprint. Discussion started: 26 October 2020

relevant publications (Wu et al., 2008, 2010; Wu, 2012; Wu et al., 2013; Lu et al., 2013; Wu et al., 2019; Lu et al., 2020a; Wu et al., 2020). The dynamic core in BCC-AGCM3-MR uses the spectral framework as described in Wu et al. (2008), in which explicit time difference scheme is applied to vorticity equation, semi-implicit time difference scheme for divergence, temperature, and surface pressure equations, and semi-Lagrangian tracer transport scheme is used for water vapor, liquid cloud water and ice cloud water. The main model physics in BCC-AGCM3-MR was described in Wu et al. (2019), which includes the modified scheme of deep convection suggested by Wu (2012), a new diagnostic scheme of cloud amount (Wu et al, 2019), shallow convection transport scheme (Hack, 1994), the stratiform cloud microphysics followed the framework of non-convective cloud processes in NCAR Community Atmosphere Model version 3 (CAM3, Collins et al., 2004) but a noticeable treatment for indirect effects of aerosols through mechanisms of clouds and precipitation, the radiative transfer parameterization that originally implemented in CAM3, a modified boundary layer turbulence parameterization based on the eddy diffusivity approach (Holtslag and Boville, 1993), and treatments of gravity waves that are generated by a variety of sources including orography and convection (Lu et al., 2020a).

The atmospheric component in BCC-CSM2-HR is the newly-developed version of high resolution BCC-AGCM3-HR. Main differences between BCC-AGCM3-HR and BCC-AGCM3-MR are listed in Table 1, and we will detail them in the following sections. They respectively used a spatially-variable divergence damping scheme, amelioration of Wu's deep convective scheme (Wu, 2012), and integrated consideration for shallow convection and boundary layer processes.

a. Spatially-variable divergence damping

The performance of a climate model is largely determined by complex motions at different spatial-temporal scales and interaction of these scales. Subgrid-scale motions are generally caused by high-frequency waves, and they can exert impacts on the computational stability especially for a high-resolution model. Horizontal

https://doi.org/10.5194/gmd-2020-284
Preprint. Discussion started: 26 October 2020

divergence damping is often used to control numerical noise in weather forecast models and for numerical stability reasons (Dey, 1978; Bates et al., 1993; Whitehead et al., 2011).

In BCC-AGCM, a second-order and a fourth-order horizontal Laplacians (∇^2 and ∇^4) are used to realize the damping operation on the divergence field D:

$$\frac{\partial D}{\partial t} = \cdots + k_2 \nabla^2 D, \tag{1}$$

and

$$\frac{\partial D}{\partial t} = \cdots - k_4 \nabla^4 D, \tag{2}$$

where k_2 and k_4 express the damping coefficient for the second-order and fourth-order dissipation operators, respectively. They are generally set as constant parameters. The second-order damping is used for the top three layers and the fourth-order damping for other layers.

Whitehead et al. (2011) proposed a horizontal divergence damping scheme that works on a latitude–longitude grid by using a linear von Neumann analysis. Here, we extended their idea to the spectral dynamic core in our high-resolution model BCC-AGCM3-HR, and we use a second-order horizontal damping operator with spatially-variable damping coefficient. In order to express the spacing dependence of the dissipation, an additional term is introduced in Eqs. (1) and (2) as:

$$\frac{\partial D}{\partial t} = \cdots + k_2 \nabla^2 D + k_v \nabla^2 D \tag{3}$$

and

$$\frac{\partial D}{\partial t} = \cdots - k_4 \nabla^4 D + k_v \nabla^2 D. \tag{4}$$

where

$$k_v = C_s \frac{[A_E \Delta\emptyset] \cdot [A_E \Delta\lambda]}{\Delta t}. \tag{5}$$

Here, k_v is dependent on the time-step Δt and grid spacing. A_E in Eq. (5) is the radius of the earth. $\Delta\emptyset$ and $\Delta\lambda$ stand for the latitudinal and longitudinal grid spacings, respectively. The parameter C_s is designed to depend on vertical position as,

$$C_s = C_{s0} \max\langle 1, 8\left\{1 + \tanh\left[\ln\left(\frac{p_{top}}{p_k}\right)\right]\right\}\rangle,$$

https://doi.org/10.5194/gmd-2020-284
Preprint. Discussion started: 26 October 2020

where C_{s0} is a constant and related to model resolution, p_{top} and p_k are the pressures at the top layer and the kth one of the model. This dependence is to introduce a diffusive sponge layer near the model top to absorb rather than reflect outgoing gravity waves (Whitehead et al., 2011). It means that the strength and frequency of the polar instabilities increase near the model top due to this increased damping coefficient, requiring a stronger diffusive operator to remove them, perhaps in addition to the polar Fourier filter. This spatially-variable damping scheme can improve the atmospheric temperature simulation in the stratosphere at polar areas of both hemispheres. This is possibly much more damping the meridional wave, as Whitehead et al. (2011) pointed out employing a damping coefficient that neglects the latitudinal variation of the grid cell area will likely damp these meridional waves more effectively.

b. Deep convection

In previous version of BCC-AGCM3-MR used in BCC-CSM2-MR, a modified scheme of deep cumulus convection developed by Wu (2012) is used (Wu et al., 2019). It is characterized as:

(1) Deep convection is initiated at the level of maximum moist static energy above the boundary layer, and the convection is triggered only when the boundary layer is unstable or there exists updraft velocity in the environment at the lifting level of convective cloud, and simultaneously there is positive convective available potential energy (CAPE).

(2) A bulk cloud model is used to calculate the convective updraft with consideration of budgets for mass, dry static energy, moisture, cloud liquid water, and momentum, and the entrainment/detrainment amount for the updraft cloud parcel is determined according to the increase/decrease of updraft parcel mass with altitude.

(3) The convective downdraft is assumed to be saturated and originated from the level of minimum environmental saturated equivalent potential temperature within the updraft cloud.

(4) The closure scheme determines the mass flux at the base of convective cloud,

https://doi.org/10.5194/gmd-2020-284
Preprint. Discussion started: 26 October 2020

and depends on the decrease/increase of CAPE resulting from large-scale processes.

Along with increasing resolution in BCC-AGCM3-HR, the detrained cloud water can be transported to its adjacent grid boxes inside a model time step. Part of the horizontally-transported cloud water is assumed to be transferred downward to lower troposphere and the amount of downward transferred water vapor is determined by the convective cloud water change with time. These modifications of the deep convection scheme are found in favor for improving the simulation of eastward propagation of MJO in the tropics, and their details will be presented in another paper.

c. Boundary layer turbulence

BCC-CSM2-HR employs the University of Washington Moist Turbulence (UWMT) scheme as proposed in Bretherton and Park (2009) to replace the dry turbulence scheme of Holtslag and Boville (1993). The latter was used in BCC-CSM2-MR. In UWMT, the first-order K diffusion is used to represent all turbulences, by which the turbulent fluxes of a variable χ are written as

$$\overline{w'\chi'} = -K_\chi \frac{\partial \chi}{\partial z} \quad . \qquad (6)$$

The eddy diffusivity, Kχ, is calculated based on the turbulent kinetic energy (TKE, e) and proportional to the stability-corrected length scale lS_χ, given by

$$K_\chi = lS_\chi \sqrt{e} \quad . \qquad (7)$$

In the case of an inversion layer at the top of convective BLs, the diffusivity is parameterized with

$$K_\chi = w_e \Delta z_e \, , \qquad (8)$$

where w_e is the entrainment rate and Δz_e is the thickness of the entrainment layer. The UWMT scheme uses the Nicholls and Turton (1986) w* entrainment closure:

$$w_e = A \frac{w_*^3}{\left(g\Delta^E s_{vl} / s_{vl}\right)\left(z_t - z_b\right)} \quad . \qquad (9)$$

Here, w* is the convective velocity, z_t and z_b are the top and bottom heights of the entrainment layer, Δ^E denotes a jump across the entrainment layer, and svl is the liquid virtual static energy. A is a nondimensional entrainment efficiency, which is

https://doi.org/10.5194/gmd-2020-284
Preprint. Discussion started: 26 October 2020

affected by evaporative cooling of mixtures of cloud-top and above-inversion air.

Compared to dry convective BLs over land which is mainly forced by the surface heating, the structure of marine stratocumulus-topped BLs depends strongly on dominant turbulence generating mechanism resulting from both evaporative and radiative cooling at cloud top. The UWMT scheme aims to provide a more physical and realistic treatment of marine stratocumulus-topped BLs and it has been demonstrated that the observed patterns of low-cloud amount with maxima in the subtropical stratocumulus decks can be well reproduced by UWMT in the Community Atmosphere Model (Park and Bretherton, 2009). The implementation of the UWMT scheme in BCC-CSM2-HR is aimed to improve the simulation of the low-level clouds over subtropical eastern oceans and these improvements are found critical to reduce the double-ITCZ bias of precipitation (Lu et al., 2020b).

d. **Shallow convection**

BCC-CSM2-HR basically inherits the shallow convection parameterization used in BCC-CSM2-MR, which is a stability-dependent mass-flux representation of moist convective processes with the use of a simple bulk three-level cloud model, as in Hack (1994). Specifically, in a vertically discrete model atmosphere where the level index k decreases upward and considering the case where layers k and k+1 are moist adiabatically unstable, the Hack scheme assumes the existence of a non-entraining convective element with roots in level k+1, condensation and rain out processes in level k, and limited detrainment in level k-1. By repeated application of this procedure from the bottom of the model to the top, the thermodynamic structure is locally stabilized.

The Hack shallow cumulus scheme can be also active in moist turbulent mixing, such as stratocumulus entrainment, which has different physical characteristics than cumulus convection. Shallow cumulus is usually regarded as a decoupled BL regime in which the vertical mixing processes do not achieve a single well-mixed layer, while the stratocumulus regime represents a well-mixed BL up to cloud top. The decoupling criterion to distinguish between the two regimes is of great importance for simulating

https://doi.org/10.5194/gmd-2020-284
Preprint. Discussion started: 26 October 2020

the stratocumulus-to-cumulus transition (Bretherton and Wyant, 1997; Wood and Bretherton, 2004). A number of these decoupling criteria have been explored, such as static stability (Klein and Hartmann, 1993) and buoyancy flux integral ratio (Turton and Nicholls, 1987). In the light of its robustness, the stability criterion with a threshold of 17.5 K is introduced into the Hack scheme. The lower tropospheric stability (LTS) is defined as

$$LTS = \theta_{700hPa} - \theta_{sfc}, \tag{10}$$

where θ_{700hPa} and θ_{sfc} are potential temperatures at 700 hPa and surface, respectively. In BCC-CSM2-HR, the modified Hack scheme is activated only in the decoupled BL regimes with $LTS < 17.5$ K to remove adiabatically moist instability. This modification to the triggering of shallow convection is found to improve the simulation of the ITCZ precipitation (Lu et al., 2020b).

2.2 Land surface model

The land surface component of BCC-CSM2-MR and BCC-CSM2-HR is the Beijing Climate Center Atmosphere-Vegetation Interaction Model (BCC-AVIM). It is a comprehensive land surface scheme developed and maintained in BCC. The version 1 (BCC-AVIM1.0) was used as the land component in BCC-CSM1.1m participating in CMIP5 (Wu et al., 2013). The land component in BCC-CSM2-MR is BCC-AVIM version 2.2 (Li et al., 2019). It includes major land surface biophysical and plant physiological processes (Ji, 1995; Ji et al., 2008), with 10 layers for soil and up to five layers for snow. The details may refer to Li et al. (2019). The main difference between BCC-AVIM2.2 and BCC-AVIM2.3 is in the sub-grid surface classification.

2.3 Ocean and Sea Ice Models

The ocean component of BCC-CSM2-HR is MOM5 (Modular Ocean Model, version 5.1) developed by the Geophysical Fluid Dynamics Laboratory (GFDL, Griffies, 2012). The model is based on the hydrostatic primitive equations and uses the Boussinesq approximation. The model uses Arakawa B-grid in the horizontal, with a globally uniform 0.25°resolution. The quasi-horizontal rescaled height

https://doi.org/10.5194/gmd-2020-284
Preprint. Discussion started: 26 October 2020

coordinate, namely, z* vertical coordinate is employed for enhancing flexibility of model applications and comforts of algorithms. There are 50 levels in the vertical, with a resolution of 10 m in the upper ocean and 367 m at the ocean bottom. The tracer advection scheme used in both the horizontal and vertical is the multi-dimensional piecewise parabolic method (MDPPM), which is of higher order and more accurate (less dissipative). MOM5 has a complete set of physical processes with advanced parameterization schemes. Effect of mesoscale eddies is taken into account through the neutral diffusion scheme of Griffies et al. (1998) with a constant diffusivity of 800 $m^2 s^{-1}$ and the neutral slope tapering scheme of Danabasoglu and McWilliams (1995) with the maximum slope of 1/200. The K-profile parameterization (KPP) is used to parameterize ocean surface boundary layer processes (Large et al., 1994). MOM5 uses the optical scheme of Manizza et al. (2005) to define the light attenuation exponentials. SeaWiFS chlorophyll-a monthly climatology is used in the calculation of the attenuation of shortwave radiation entering the ocean layers with a maximum depth set at 200m. The re-stratification effects of sub-mesoscale eddies in the ocean surface mixed layer are parameterized with the sub-mesoscale scheme of Fox-Kemper et al. (2008) and Fox-Kemper et al. (2011). The ocean component of BCC-CSM2-MR is MOM4-L40, also developed by the GFDL (Griffies et al., 2005). It has a nominal resolution of 1°x1° with a tri-pole grid, and the actual resolution is from 1/3° latitude between 10°S and 10°N to 1° at 60° latitude. There are 40 levels in the vertical. More details are referred to Wu et al. (2019). The sea-ice component of BCC-CSM2-HR and BCC-CSM2-MR is SIS (Sea Ice Simulator) developed by GFDL (Delworth et al., 2006). SIS employs Semtner's scheme for the vertical thermodynamics and contains full dynamics with internal ice forces calculated using an elastic-viscous-plastic rheology. SIS has three vertical layers, including one snow cover and two ice layers of equal thickness. The sea-ice component operates on the same oceanic grid and has the same horizontal resolution.

3. Experimental design and simulations

The principal simulation to be analyzed is the historical simulation (hereafter

https://doi.org/10.5194/gmd-2020-284
Preprint. Discussion started: 26 October 2020

historical) with prescribed forcings from 1971 to 2000 for both BCC-CSM2-MR and BCC-CSM2-HR. All historical forcings are from the CMIP6-recommended data (https://esgf-node.llnl.gov/search/input4mips/) including: (1) Greenhouse gases concentrations such as CO_2, N_2O, CH_4, CFC11 and CFC12 with zonal-mean values and updated monthly; (2) Annual means of total solar irradiance derived from the CMIP6 solar forcing; (3) Stratospheric aerosols from volcanoes; (4) CMIP6-recommended tropospheric aerosol optical properties due to anthropogenic emissions that are formulated in terms of nine spatial plumes associated with different major anthropogenic source regions using version 2 of the Max Planck Institute Aerosol Climatology Simple Plume model (MACv2-SP, Stevens et al., 2017); (5) Time-varying gridded ozone concentrations; (6) Yearly global gridded land-use forcing. In addition, aerosol masses based on CMIP5 (Taylor et al., 2012) are also used for the on-line calculation of cloud droplet effective radius in our models.

The historical simulation of BCC-CSM2-MR follows the requirement of CMIP6. The preindustrial initial state is obtained after a 500-year piControl simulation, and the historical simulation is then conducted from 1850 to 2014 (Wu et al., 2019). The simulation of BCC-CSM2-HR covers the historical period from 1950 to 2014. Its initial state is the final state from a 50-year control simulation with fixed historical forcing of the year 1950, following the HighResMIP protocol. The control run itself is initiated from the states of individual components with their uncoupled mode. That is, the state of atmosphere and land are obtained from a 10-year AMIP run forced with monthly climatology of sea surface temperature (SST) and sea ice concentration, while the states of ocean (MOM5) and sea ice (SISv2) are derived from a 1000-year forced run with a repeating annual cycle of monthly climatology of atmospheric state from the Coordinated Ocean-Ice Reference Experiment (CORE) dataset version 2 (Danabasoglu et al., 2014).

4. Results

In order to fairly evaluate BCC-CSM2-MR and BCC-CSM2-HR against observation-based or reanalysis data, and to make a right inter-comparison among the

https://doi.org/10.5194/gmd-2020-284
Preprint. Discussion started: 26 October 2020

three models, we choose a common period of 30 years from 1971 to 2000 from their historical simulations in this work.

4.1 Global energy budget

Satellite observation is a direct monitoring of the net radiation at top-of-atmosphere (TOA, Wielicki et al, 1996), which is a primary indicator for the Earth's energy balance. CERES-EBAF products are derived on the basis of satellite observation data from CERES (Clouds and Earth's Radiant Energy System) project and synthesized with EBAF (Energy Balanced and Filled) data, suitable for evaluation of climate models. The 2001-2014 monthly global gridded net radiations at top-of-atmosphere (TOA) from CERES-EBAF products are used to evaluate the two versions of BCC-CSM. As shown in Table 2, the globally-averaged TOA net energy is 1.81±0.49 W·m^{-2} in BCC-CSM2-MR and 1.08±0.46 W·m^{-2} in BCC-CSM2-HR for the period from 1971 to 2000. The energy equilibrium of the whole earth system in BCC-CSM2-HR is slightly improved. The TOA shortwave and longwave components in BCC-CSM2-HR are much closer to CERES-EBAF than BCC-CSM2-MR. It is to be noted that only the period 2001–2014 is available for CERES-EBAF. We believe it is still a good climatology to evaluate our models despite the lack of temporal concomitance.

Clouds constitute a major modulator of the radiative transfer in the atmosphere, and their radiative properties exert strong impacts on the equilibrium and variation of the radiative budget at TOA. The globally-averaged shortwave cloud radiative forcing in BCC-CSM2-MR and BCC-CSM2-HR are slightly stronger than that in CERE-EBAF (-47.16±0.24 W·m^{-2}) about 3 W·m^{-2} of cooling effect, and the globally-averaged longwave cloud radiative forcing in the two models are also stronger than the CERE-EBAF data (25.99±0.25 W·m^{-2}) near 2 W·m^{-2} of warming effect. The obvious biases of model with contrast to CERE-EBAF are mainly located in the mid-latitudes and subtropics. Figure 2 shows annual and zonal mean of shortwave, longwave and net cloud radiative forcing for the two model versions and observations. The longwave and net cloud radiative forcing are overall consistent with

https://doi.org/10.5194/gmd-2020-284
Preprint. Discussion started: 26 October 2020

CERE-EBAF in most latitudes. In mid-latitudes of both the hemispheres, the shortwave cloud radiative forcing from BCC-CSM2-HR is much closer to CERE-EBAF than that from BCC-CSM2-MR. But in low latitudes between 30°S and 30°N, BCC-CSM2-HR simulates excessive cloud shortwave radiative forcing which mainly comes from evident biases over the eastern tropical Pacific and tropical Atlantic oceans (Figure 3). These biases are possibly attributable to the new scheme of boundary layer processes in which abundant water vapor are confined in the lower atmosphere in those regions.

4.2 Vertical structure of the atmosphere temperature and wind

Figure 4 presents zonally averaged vertical profiles of air temperature and zonal wind for December-January-February (DJF) and June-July-August (JJA) as simulated by BCC-CSM2-MR and BCC-CSM2-HR, with contrast to the ERA5 reanalysis below the 1-hPa level (Hersbach and Dee 2016) and climatological values above the 1-hPa level from the COSPAR (Committee on Space Research) International Reference Atmosphere (CIRA86, Fleming et al., 1990), in which all data except CIRA86 are time averaged over the period from 1971 to 2000. The air temperature in DJF is characterized as cool layers centralized near about 300 hPa in the Northern Hemisphere and too warm layers near 1 hPa in the Southern Hemisphere. Those different vertical structures in both hemispheres during DJF are almost reversed of JJA. They are clear in BCC-CSM2-HR. The warmer layer over top of the stratosphere near 1 hPa cannot be captured in BCC-CSM2-MR as its top is limited at 1.456 hPa.

Figure 5 shows biases of the zonally-averaged annual air temperature, relative to ERA5. Here only model data from 5 hPa to 1000 hPa are evaluated as there are spare station-based observations above 5 hPa and it is generally recognized that most of stations don't reach their best-practice altitude of 5 hPa (https://gcos.wmo.int/en/atmospheric-observation-panel-climate). Lower troposphere temperature biases are relatively small. The two models BCC-CSM2-MR and BCC-CSM2-HR have a negative air temperature bias that appears above the 250 hPa pressure level (Fig. 5) in the subpolar and polar region, but a positive bias above 150 hPa in tropical regions. A prominent cold bias in the lower stratosphere and the upper troposphere does not decrease in magnitude at higher horizontal resolution, and such a negative bias in the troposphere has already been reported in many CMIP5 models (see Charlton-Perez et al., 2013; Tian et al., 2013). In the upper stratosphere, all model versions exhibit a warm bias that is maximal in the mid-latitudes and relatively insensitive to changes in atmospheric resolution.

As shown in Figure 4, the basic pattern of vertical structures of westerly and easterly zones and their changes in DJF and JJA are generally well simulated by BCC-CSM2-MR and BCC-CSM2-HR. Both models have westerly wind biases of annual means that are located in the upper troposphere and stratosphere near 60°S and 60°N (Figures 5b and 5d), and reflect the meridional structure of temperature biases (Figures 5a and 5c) in accordance with the thermal–wind relationship. The largest biases in westerly winds near 100hPa in the tropics may be related to the QBO and its downward propagation.

4.3 Surface Climate

Precipitation, land surface air temperature and sea surface temperature, sea-ice concentration are important variables, and there are rich ground- or satellite-based observations suitable for the assessment of model performance in terms of mean climate.

4.3.1 Precipitation

Observed monthly precipitation is taken from the Global Precipitation Climatology Project (GPCP version 2.2; Adler et al., 2003) data set at 2.5° resolution for the period 1981−2010. Figure 6 shows the spatial distribution of DJF and JJA mean precipitation for BCC-CSM2-MR and BCC-CSM2-HR, compared to GPCP. The two versions of BCC-CSMs were both able to reproduce the global observed precipitation patterns and there is an evident improvement in the high-resolution model (BCC-CSM2-HR). Improvements are particularly clear in the Pacific, Indian, and Atlantic Oceans. The double-ITCZ issue is one of the most significant biases that persists in many climate models (e.g., Hwang and Frierson, 2013; Li and Xie, 2014).

It exists in BCC-CSM2-MR, with excessive precipitation in the South Pacific Convergence Zone (SPCZ). This bias almost disappears in BCC-CSM2-HR. A strong negative bias of JJA precipitation over the Amazon region exists in the two models. As shown in Figure 7, there is too much precipitation along the southern intertropical convergence zone (ITCZ) in BCC-CSM2-MR, which is mainly caused by excessive precipitation in the southern intertropical zone in DJF. This systematic bias is evidently improved in BCC-CSM2-HR. But the intensity of precipitation in the northern intertropical convergence zone in BCC-CSM2-HR is stronger than that from GPCP, which is partly attributed to the excessive precipitation in the tropical oceans, especially in the eastern tropical North Pacific (Figure 6e).

The 2001-2019 quasi-global (60° N–60° S) 0.1° × 0.1° gridded half-hourly precipitation estimates of Global Precipitation Measurement (GPM) Integrated Multi-satellitE Retrievals for GPM (IMERG) products are used to evaluate the precipitation intensity in BCC-CSMs. IMERG data are rainfall estimates combining data from all passive-microwave instruments in the GPM Constellation, together with microwave-calibrated infrared satellite estimates, precipitation gauge analyses, and potentially other precipitation estimators at fine time over the entire globe (Huffman et al., 2019). Figure 8 shows the probability density of hourly precipitation in function of precipitation intensity with intervals of 1 mm/hour between 40°S and 40°N. The frequency of events with precipitation rate smaller than 1 mm/hour in the two versions of BCC-CSMs is both higher than in IMERG data, but lower for precipitation rate exceeding 10 mm/hour. This is a common bias in global climate models raising concerns for any studies on precipitation extremes. Compared to BCC-CSM2-MR, BCC-CSM2-HR with resolution increased shows obvious improvement for its ability to capture the spectral distribution of precipitation, especially the contrast between heavy and light rains.

4.3.2 Near-surface temperature

Global monthly mean sea surface temperature (SST) from 1971 to 2000 is taken from the EN4 objective analysis (Good et al., 2013), and land surface air temperature at 2 m is derived from the Climatic Research Unit (CRU) data set (Harris et al., 2013). Figure 9 shows a spatial-distribution map of the annual mean SST for EN4 and the biases for BCC-CSM2-MR and BCC-CSM2-HR relative to EN4. BCC-CSM2-MR is generally warmer, while BCC-CSM2-HR is colder than what observed. A warm SST bias in BCC-CSM2-MR spreads throughout most oceans, except the north Pacific and north Atlantic. Such warm biases do not appear in BCC-CSM2-HR, and the cold SST biases in the eastern subtropical south Pacific are possibly attributed to excessive clouds there, also manifested by strong cloud shortwave radiative forcing. The warm biases in the eastern tropical ocean basins in BCC-CSM2-MR are associated with a deficit of stratiform low-level clouds, a common and systematic bias for many climate models (Richter, 2015). The cold biases there in BCC-CSM2-HR, similarly, are associated with too much low cloud, except over the tropical north Pacific.

Figure 10 shows the simulation biases of annual mean land-surface air temperature from BCC-CSM2-MR and BCC-CSM2-HR. The near-surface air temperature over land in BCC-CSM2-MR is generally cooler than the CRU observations, particularly exhibiting severe cool biases in North Europe. Increasing atmospheric resolution in BCC-CSM2-HR does not seem to show amelioration, and the surface air temperatures in BCC-CSM2-HR exhibits rather similar patterns for their biases in BCC-CSM2-MR and there are biases of -2 to 2 K in most land regions between 50°N and 50°S with contrast to CRU data.

4.3.3 Sea ice

Figure 11 shows the annual mean sea ice concentration simulated by BCC-CSM2-MR and BCC-CSM2-HR over the period 1971–2000, compared to the climatology (1971–2000) from Hadley Centre Sea Ice and Sea Surface Temperature data set (HadISST, Rayner et al., 2003). The simulated geographic distribution of sea ice in the Arctic is overall realistic, except that the sea ice concentration in the Atlantic is slightly overestimated in both models. This overestimation of sea ice possibly has a consequence for the severe cold biases of surface air temperature in North Europe (Figure 10). In the Antarctic, sea ice concentration simulated by

Geoscientific Model Development
Discussions

BCC-CSM2-MR is smaller than HadISST data, especially from 60°W to 60°E in the subpolar region where the simulated SST is warmer compared to EN4 (Figure 9b). Those deficiencies in BCC-CSM2-MR are largely improved in BCC-CSM2-HR (Figure 11f).

Figure 12 shows the monthly sea ice covers for the Arctic and Antarctic from BCC-CSM2-MR and BCC-CSM2-HR. HadISST observations show that the Arctic sea ice cover reaches a minimum extent of 6.9×10^6 km^2 in September and rises to a maximum extent of 16.0×10^6 km^2 in March, and the Antarctic sea ice cover reaches a minimum extent in February and a maximum extent in September. The seasonal cycle amplitude and phase of sea ice area are well captured by the two models, and their biases are almost smaller than 1×10^6 km^2 while compared to HadISST observations. We note that the extents of the Arctic sea ice for each month in BCC-CSM2-MR are slightly but systematically smaller than HadISST, and in the Antarctic are less in February and March but larger in other months than HadISST. BCC-CSM2-HR slightly overestimated sea ice concentration about 1×10^6 km^2 in both hemispheres with reference to HadISST.

4.4 Tropical Climate

The tropical cyclone (TC), also known as typhoon or hurricane, is among the most destructive weather phenomena. The Madden-Julian Oscillation (MJO) is the dominant mode of sub-seasonal variability in the tropical troposphere (Madden and Julian, 1971), and the quasi-biennial oscillation (QBO) is a quasiperiodic oscillation of the equatorial zonal wind between easterlies and westerlies in the tropical stratosphere. TC, MJO and QBO are very important variabilities in the tropics, with consequences to global weather and climate.

4.4.1 Tropical Cyclones

Following previous studies (Murakami, 2014), we use multiple criteria to detect TCs in our simulations. (1) The maximum of daily relative vorticity of a TC-like vortex at 850 hPa exceeds 15×10^{-5} s^{-1} for BCC-CSM2-HR and 1×10^{-5} s^{-1} for BCC-CSM2-MR; (2) The warm-core above the TC-like vortex, which is presented as the sum of the air temperature deviations at 300, 500 and 700 hPa over a 10°×10° grid box, exceeds 0.8 K; (3) The maximum wind speed at 850 hPa is higher than that at 300 hPa; (4) The maximum wind speed within the TC-like vortex center 3°×3° grid box is higher than 10 m s^{-1}; (5) The genesis position of the TC-like vortex is over the ocean; (6) The duration of the TC-like vortex satisfied above conditions exceeds 48 hours.

In Figure 13, we evaluate the average TC frequency over the twenty years (1981-2000) from BCC-CSM2-MR and BCC-CSM2-HR, with contrast to the climatology (1981–2000) of observations from International Best Track Archive for Climate Stewardship (IBTrACS; Knapp et al., 2010). It is clear that TC activity is increased with resolution enhanced. The averaged total global TC numbers per year are 58.3 in BCC-CSM2-MR and 92.3 in BCC-CSM2-HR, and are slightly larger than IBTrACS observation (89.7), although one of the above criteria for TC in BCC-CSM2-MR is looser than that in BCC-CSM2-HR. Spatially, BCC-CSM2-HR generates excess TC activity in the eastern North Pacific, Northern Indian Ocean, and Southern Hemisphere. But both models severely underestimate TC activity in the North Atlantic and in the Caribbean Sea. The general overestimation of TC activity in the eastern North Pacific and over the opposite in the North Atlantic in BCC-CSM2-HR may be related to the warmer SST in the eastern tropical North Pacific and colder SST in the tropical Atlantic with contrast to EN4 data (Figure 9c), but other factors such as the entrainment in the parameterization of convection may also have an influence (Zhao et al., 2012). The biases of missing TC activity in the North Atlantic also exist in other models (e.g., Bell et al., 2013; Strachan et al., 2013; Small et al., 2014), and still remain a challenge for the climate modelling community.

Figure 14 shows the maximum surface wind speed versus minimum sea level pressure for the tropical cyclones that are derived from the 1981-2000 daily IBTrACS observation (black dots and line), and from the 1981-2000 daily simulations of BCC-CSM2-MR and BCC-CSM2-HR. Consistent with other similar studies (e.g., Yamada et al., 2017), BCC-CSM2-MR and BCC-CSM2-HR cannot capture weak storms whose maximum wind speeds are less than 10 m·s^{-1}. The maximum wind speed for TC in BCC-CSM2-MR only reaches to 30 $m \cdot s^{-1}$. BCC-CSM2-HR, as expected, can reproduce those strong TCs for which daily mean minimum pressure in TC centers may reach to 960 hPa and daily mean maximum wind speed may reach to 50 $m \cdot s^{-1}$. The fitting line of maximum wind speeds with minimum center pressures in BCC-CSM2-HR almost matches that from IBTrACS observation (Figure 14).

4.4.2 Madden–Julian Oscillation

MJO is characterized by eastward propagation of deep convective structures moving along the Equator with an average phase speed of around 5 $m \cdot s^{-1}$ at the intraseasonal time scale of 20–100 days (Wheeler and Kiladis, 1999). MJO generally forms over the Indian Ocean, strengthens over the Pacific Ocean, and weakens due to interaction with South America and cooler eastern Pacific SSTs (Madden and Julian, 1971). Figure 15 gives the lag-longitude evolution of 10°S–10°N-averaged intraseasonal precipitation anomalies and lag-longitude evolution of 80°–100°E-averaged intraseasonal precipitation anomalies correlated against the precipitation over the equatorial eastern Indian Ocean. Both versions of BCC-CSMs reasonably reproduce the eastward propagating feature of convection from the Indian Ocean across the Maritime Continent to the Pacific (Figs. 15b and 15c), as well as apparent poleward propagations from the equatorial Indian Ocean into the Northern Hemisphere and the Southern Hemisphere (Figs. 15e and 15f). The northward propagation is more skillfully depicted in simulations in BCC-CSM2-HR than in BCC-CSM2-MR. The average phase speed of eastward propagation of deep convection in BCC-CSM2-HR is much closer to the GPCP data denoted by the dashed line in Fig 15c. Figure 15b shows that the eastward propagation of deep convection in BCC-CSM2-MR is too fast, compared to GPCP data.

MJO activity can be generally featured by a life cycle of eight phases (Wheeler and Hendon, 2004). Intensity of outgoing longwave radiation (OLR) is often used for this purpose to represent the activity of convection. Figure 16 shows the MJO phase-latitude diagram of composited outgoing longwave radiation (OLR) and 850-hPa zonal wind anomalies averaged over 10°S–10°N. Here, on the basis of extracting the leading multivariate empirical orthogonal functions (EOFs) and principal components (PCs) of intra-seasonal OLR, 850-hPa and 200-hPa zonal wind anomalies, eight MJO phases are defined by the inverse tangent of the ratio of PC2 to PC1 as in Wheeler and Hendon (2004). In observation, MJO convection initiated from Africa and the western Indian Ocean at phases 1–2, propagates eastward from the Indian Ocean across the Maritime Continent to the western Pacific at phases 3–6, and finally disappears in the western hemisphere at phases 7–8. BCC-CSM2-MR generally captures the evolution of convection with MJO phases, but shows faster propagative speed and apparently underestimates the intensity compared to the observation. In contrast, BCC-CSM2-HR shows an obviously improved MJO phase transition and convection intensity.

4.4.3 The stratospheric quasi-biennial oscillation

The alternative oscillation between westerly and easterly winds in the tropical stratosphere constitutes the characteristic feature of the quasi-biennial oscillation (QBO). The good simulation of QBO still remains nowadays a challenge for all state-of-the-art climate models. In a recent work, Kim et al. (2020) showed that only half (15 out of 30) of the CMIP6 models can internally generate QBO (BCC-CSM2-MR was in the good half). We should however recognize that there was a huge progress in CMIP6, since in CMIP5 only five models (about 10% of the total) were able to simulate a realistic QBO (Schenzinger et al., 2017).

To evaluate model performance in simulating the QBO, the time-height cross sections of the tropical zonal winds averaged from 5°S to 5°N for BCC-CSM2-MR and BCC-CSM2-HR are compared with contrast to the ERA5 reanalysis. As shown in Figure 17, ERA5 shows alternative westerlies and easterlies in the lower stratosphere with a mean periodicity of about 28 months. The two BCC models are both able to generate a reasonable QBO, and the observed asymmetry in amplitude with the easterlies being stronger than the westerlies are also well reproduced. The general performance of QBO in BCC-CSM2-MR was evaluated in Wu et al. (2019). A detailed assessment of the underlying mechanism involving wave dynamics and the associated forcing to drive QBO is presented in Lu et al. (2020a). The simulated QBO has stronger amplitudes in BCC-CSM2-HR than in BCC-CSM2-MR. As the

https://doi.org/10.5194/gmd-2020-284
Preprint. Discussion started: 26 October 2020

horizontal resolution and physics package are changed from BCC-CSM2-MR to BCC-CSM2-HR, the parameterized convective gravity wave forcing for QBO seems enhanced in BCC-CSM2-HR. On the other hand, changes in the convective cumulus parameterization can also affect the simulation of the resolved convectively coupled equatorial waves (i.e., the Kelvin wave) driving the QBO, and lead to stronger QBO amplitudes in BCC-CSM2-HR.

In the two BCC models, the downward propagation of QBO occurs in a regular manner, but does not sufficiently penetrate to low altitudes below 50 hPa. The vertical resolution is similar below ~10 hPa in both BCC-CSM2-MR and BCC-CSM2-HR (Figure 1). A further downward propagation to lower altitudes can be expected by increasing the vertical resolution finer than 500 m to adequately resolve the wave-mean flow interaction in the upper troposphere-lower stratosphere (Geller et al. 2016; Garcia and Richter 2019).

4.4.4 Niño3.4 SST variability

Figure 18 presents time series of the monthly Niño3.4 SST (5°N−5°S, 170°W−120°W) anomalies from BCC-CSM2-MR and BCC-CSM2-HR, with reference to EN4 data from 1971 to 2000. The amplitude of interannual variation of the Nino3.4 index in BCC-CSM2-HR is weaker than in EN4 and in BCC-CSM2-MR. The power spectrum analysis of the Niño3.4 index from the EN4 observations shows significant peaks at 4-6 years and 2-3 years. The periodicity of the ENSO cycle in BCC-CSM2-MR is mainly at 2-3 years. It is prolonged to 3-4 years in BCC-CSM2-HR. In Figure 18e, the El Niño SST variability from EN4 data reaches its maximum in the period from November to January. The phase locking simulated by BCC-CSM2-MR occurs in autumn. The simulated ENSO phase locking in BCC-CSM2-HR is partly improved and the ENSO events tend to reach their maximum toward winter, in spite of two months lag in the peak time.

Figure 19 presents the spatial patterns of correlation coefficients between the Niño3.4 index and global SST anomalies from 1971 to 2000 for the EN4 observation and the two BCC models. Both BCC-CSM2-HR and BCC-CSM2-MR simulate a positive correlation structure over the equatorial region of the central and eastern

https://doi.org/10.5194/gmd-2020-284
Preprint. Discussion started: 26 October 2020

Pacific, which is consistent with the analysis from EN4 despite of a too-westward extension into the western Pacific. The EN4 data show clearly that the zone of positive correlation of SST with the Niño3.4 index in the equatorial eastern Pacific expands to extra-tropics. There are also remarkable areas of positive correlation in the equatorial Indian Ocean and the eastern tropical Atlantic. Compared to BCC-CSM2-MR, BCC-CSM2-HR improves the simulation in those regions. We also note that areas of negative correlation of SST with the Niño3.4 index in the western equatorial Pacific extend to the south and north Pacific in EN4, a phenomenon however not clearly simulated in BCC-CSM2-HR, even deteriorated compared to BCC-CSM2-MR.

5. Conclusions

This paper was devoted to the presentation of the high-resolution version BCC-CSM2-HR and to the description of its climate simulation performance. We focused on its updating and differential characteristics from its predecessor, the medium-resolution version BCC-CSM2-MR. BCC-CSM2-HR is our model version participating to the HighResMIP, while BCC-CSM2-MR is our basic model version for other CMIP6-Endorsed MIPs (Wu et al., 2019; Xin et al. 2019).

The atmosphere resolution is increased from T106L46 in BCC-CSM2-MR to T266L56 in BCC-CSM2-HR, and the ocean resolution from 1°x1° in BCC-CSM2-MR to 1/4°x1/4° in BCC-CSM2-HR. A few novel developments were implemented in BCC-CSM2-HR for both the dynamics core and model physics in the atmospheric component. Firstly, a spatially-variable damping for the divergence field was used to improve the atmospheric temperature simulation in the stratosphere at polar areas. It helps to control high-frequency noise in the stratosphere and above. Secondly, the deep cumulus convection scheme originally described in Wu (2012) was further ameliorated to allow detrained cloud water be transported to adjacent grids and downward to lower troposphere. Thirdly, we modified the relevant schemes for the boundary layer turbulence and shallow cumulus convection to improve the simulation of ITCZ precipitation. Finally the UWMT scheme is used to improve the simulation of the low-level clouds over eastern basins of subtropical oceans. The land

https://doi.org/10.5194/gmd-2020-284
Preprint. Discussion started: 26 October 2020

model configuration in BCC-CSM2-HR is the same as that in BCC-CSM2-MR. Major land surface biophysical and plant physiological processes of BCC-AVIM2 implemented in BCC-CSM2-MR and BCC-CSM2-HR keep the same, and main differences are in the sub-grid surface classification. The ocean component of BCC-CSM2-HR is upgraded from MOM4 in BCC-CSM2-MR to MOM5. The sea ice component is also updated from SIS4 in BCC-CSM2-MR to SIS5 in BCC-CSM2-HR.

For the sake of a rigorous comparison, two simulations of 30 years each were realized under the same historical conditions from 1971 to 2000 with BCC-CSM2-MR and BCC-CSM2-HR, respectively. We compared the basic climate features in relation to atmospheric temperature, circulation, precipitation, surface temperature, and sea ice between the two simulations and we evaluated them against observation-based and reanalysis data. With contrast to the medium-resolution BCC-CSM2-MR, the high-resolution BCC-CSM2-HR has a slightly improved energy equilibrium for the whole earth system. The global mean TOA net energy balance is about 1.08 $W \cdot m^{-2}$ in BCC-CSM2-HR for the period from 1971 to 2000, showing an evident improvement compared to 1.81 $W \cdot m^{-2}$ in BCC-CSM2-MR. The longwave and net cloud radiative forcing are overall consistent with CERE-EBAF in most latitudes, but excessive cloud radiative forcing for shortwave radiation is found over the eastern tropical Pacific and tropical Atlantic in BCC-CSM2-HR. Lower troposphere temperature biases are relatively small. Both versions of BCC-CSMs have a cold air temperature bias that appears above 250 hPa in the subpolar and polar region, and a warm bias in the upper stratosphere in the mid-latitudes, which caused westerly wind biases in the upper troposphere and in the stratosphere.

Although those prominent systematic biases in temperature and wind do not change at higher horizontal and vertical resolution and seems relatively insensitive to changes in atmospheric resolution, the ability to capture the winter to summer seasonal change in the vertical structure of temperature and wind in the upper stratosphere is strengthened in BCC-CSM2-HR.

The two versions of BCC-CSMs were both able to reproduce the observed global precipitation patterns and there is a remarkable improvement in precipitation centers

https://doi.org/10.5194/gmd-2020-284
Preprint. Discussion started: 26 October 2020

over the Pacific, Indian, and Atlantic Ocean in the high-resolution model. The double-ITCZ biases in BCC-CSM2-MR are reduced in BCC-CSM2-HR and excessive precipitation in the South Pacific Convergence Zone is also strongly reduced in BCC-CSM2-HR. The climatological SST in BCC-CSM2-HR, relative to the observation-based EN4 data, shows cold biases but reduced compared to BCC-CSM2-MR. Such SST cold biases are partly attributable to different ocean components, MOM4 in BCC-CSM2-MR and MOM5 in BCC-CSM2-HR. The seasonal cycles of amplitude and phase of sea ice in both hemispheres are generally well captured in BCC-CSM2-HR, but with a small excess all year round in the Northern Hemisphere, especially in the Atlantic.

We also conducted an assessment on a few important phenomena of the tropical climate, such as TC (tropical cyclone), MJO (Madden-Julian oscillation), QBO (quasi-biennial oscillation), and ENSO (El Nino – southern oscillation). The averaged total number of global TC in BCC-CSM2-HR is a bit larger than IBTrACS observation. BCC-CSM2-HR can simulate main TC activities in the eastern North Pacific, Northern Indian, and in the Southern Hemisphere but misses the TC activities in the North Atlantic. BCC-CSM2-HR is able to capture a realistic MJO signal including the eastward-propagating behavior of MJO and its phase speed. The QBO-related alternative westerlies and easterlies in the tropical lower stratosphere with a mean periodicity of about 28 months are well simulated. The weakness in downward propagation of the simulated QBO (insufficient penetration of the signal to low altitudes) in BCC-CSM2-MR is slightly improved in BCC-CSM2-HR. Main features of the ENSO cycle such as the periodicity and phase locking are captured by BCC-CSM2-HR although its main ENSO periodicity of 3-4 years is still shorter than EN4 observations and the pick time of ENSO variability is about two months later compared to EN4 data.

We finally note that there exist some systematic biases in our high-resolution model, such as excessive cloud radiative forcing for shortwave radiation over the eastern tropical Pacific, cold biases in the near surface temperature over North Europe, and over the tropical Atlantic, insufficient TC activities over the North Atlantic. These are all important issues to improve in our future model development.

Code and data availability

Source codes of BCC-CSM-HR model can be accessed at a DOI repository http://doi.org/10.5281/zenodo.4127457 (Wu et al., 2020b). Model output of BCC models for CMIP6 simulations described in this paper is distributed through the Earth System Grid Federation (ESGF) and freely accessible through the ESGF data portals after registration (http://doi.org/10.22033/ESGF/CMIP6.2921, Jie et al., 2020). Details about ESGF are presented on the CMIP Panel website at http://www.wcrp-climate.org/index.php/wgcm-cmip/about-cmip. All source code and data can also be accessed by contacting the corresponding author Tongwen Wu (twwu@cma.gov.cn).

Author contributions

Tongwen Wu led the BCC-CSM development, and all other co-authors contributed to it. Tongwen Wu, Weihua Jie, Xiaoge Xin, and Jie Zhang designed the experiments and carried them out. Tongwen Wu, Laurent Li, Yixiong Lu, Junchen Yao, and Fanghua Wu wrote the final document with contributions from all other authors.

Competing interests

The authors declare that they have no conflict of interest.

Acknowledgements

This work was supported by The National Key Research and Development Program of China (2016YFA0602100).

References:

Adler, R. F., Chang, A.: The Version 2 Global Precipitation Climatology Project (GPCP) Monthly Precipitation Analysis (1979-Present), J. Hydrometeor., 4, 1147–1167, 2003.

Bacmeister, J. T., Wehner, M. F., Neale, R. B., Gettelman, A., Hannay, C. E., Lauritzen, P. H., Caron, J. M., and Truesdale, J. E.: Exploratory high-resolution climate simulations using the Community Atmosphere Model (CAM), J. Climate, 27, 3073–3099, doi:10.1175/JCLI-D-13-00387.1, 2014.

Bates, J. R., Moorthi, S., and Higgins, R. W.: A global multilevel atmospheric model using a vector semi-Lagrangian finite difference scheme. Part I: Adiabatic formulation. Mon. Wea. Rev., 121, 244–263, 1993.

Bell, R. J., Strachan, J., Vidale, P. L., Hodges, K. I., and Roberts, M.: Response of tropical cyclones to idealized climate change experiments in a global high resolution coupled general circulation model, J. Climate, 26, 7966–7980, 2013.

Beres, J. H., Alexander, M. J., and Holton, J. R.: A method of specifying the gravity wave spectrum above convection based on latent heating properties and background wind, J. Atmos. Sci., 61, 324-337, 2004.

Birch, C. E., Marsham, J. H., Parker, D. J., and Taylor, C. M.: The scale dependence and structure of convergence fields preceding the initiation of deep convection, Geophys. Res. Lett., 41, 4769–4776, doi:10.1002/2014GL060493, 2014.

Bretherton, C. S. and Park, S.: A new moist turbulence parameterization in the Community Atmosphere Model, J. Climate, 22, 3422-3448, 2009.

Bretherton, C. S. and Wyant, M. C.: Moisture transport, lower tropospheric stability, and decoupling of cloud-topped boundary layers, J. Atmos. Sci., 54, 148-167, 1997.

Charlton-Perez, A.J., Baldwin, M.P., Birner T. et al: On the lack of stratospheric dynamical variability in low-top versions of the CMIP5 models. J Geophys Res Atmos, 118, 2494–2505. doi:10.1002/jgrd.50125, 2013.

Collins, W. D., Rasch, P.J., Boville, B.A., Hack, J. J., McCaa, J.R., Williamson, D. L., Kiehl, J. T., Briegleb, B., Bitz C., Lin S.J., Zhang, M.H., and Dai, Y.J.: Description of the NCAR community atmosphere model (CAM3). Technical Report NCAR/TN-464 + STR, National Center for Atmospheric Research, Boulder, Colorado, 226 pp, 2004.

Delworth, T. L., Rosati, A., Anderson,W., Adcroft, A. J., Balaji, V., Benson, R., Dixon, K., Griffies, S. M., Lee, H.-C., Pacanowski, R. C., Vecchi, G. A., Wittenberg, A. T., Zeng, F., and Zhang, R.: Simulated climate and climate change in the GFDL CM2.5 high resolution coupled climate model, J. Climate, 25, 2755–2781, doi:10.1175/JCLI-D-11-00316.1, 2012.

Danabasoglu, G., McWilliams, J. C.: Sensitivity of the global ocean circulation to parameterizations of mesoscale tracer transports. Journal of Climate 8, 2967–2987, 1995.

Danabasoglu, G., and Co-authors: North Atlantic simulations in Coordinated Ocean-ice Reference Experiments phase II (CORE-II). Part I: Mean States. Ocean Modelling, 73, 76-107, doi: 10.1016/j.ocemod.2013.10.005, 2014.

Delworth, T. L., Broccoli, A. J., Rosati, A., Stouffer, R. J., Balaji, V., Beesley, J. A., et al.: GFDL's CM2 global coupled climate models. Part I: Formulation and simulation characteristics. J. Climate, 19, 643–674, doi:10.1175/JCLI3629.1, 2006.

Demory, M.-E., Vidale, P.-L., Roberts, M., Berrisford, P., Strachan, J., Schiemann, R., and Mizielinski, M. S.: The role of horizontal resolution in simulating drivers of the global hydrological cycle, Clim. Dynam., 42, 2201–2225, doi:10.1007/s00382-013-1924-4, 2014.

Doi, T., Vecchi, G. A., Rosati, A. J., and Delworth, T. L.: Biases in the Atlantic ITCZ in seasonal–interannual variations for a coarse- and a high-resolution coupled climate model, J. Climate, 25, 5494–5511, doi:10.1175/JCLI-D-11-00360.1, 2012.

Dey, C.: Noise suppression in a primitive equation prediction model. Mon. Wea. Rev., 106, 159–173, 1978.

Endo, H., Kitoh, A., Ose, T., Mizuta, R., and Kusunoki, S.: Future changes and uncertainties in Asian precipitation simulated by multiphysics and multi-sea surface temperature ensemble experiments with high-resolution Meteorological Research Institute atmospheric general circulation models (MRI-AGCMs). J. Geophys. Res. Atmos., 117, D16118, doi:10.1029/2012JD017874, 2012.

Eyring, V., Bony, S., Meehl, G. A., Senior, C. A., Stevens, B., Stouffer, R. J., and Taylor, K. E.: Overview of the Coupled Model Intercomparison Project Phase 6 (CMIP6) experimental design and organization, Geosci. Model Dev., 9, 1937-1958, doi:10.5194/gmd-9-1937-2016, 2016.

Flato, G., Marotzke, J., Abiodun, B., Braconnot, P., Chou, S.C., Collins, W., Cox, P., Driouech, F., Emori, S., Eyring, V., Forest, C., Gleckler, P., Guilyardi, E., Jakob, C., Kattsov, V., Reason C. and Rummukainen M.: Evaluation of climate models; in Climate Change 2013: The Physical Science Basis (Contribution of Working Group I to the Fifth Assessment Report of the Intergovernmental Panel on Climate Change), (ed.) T.F. Stocker, D. Qin, G.-K. Plattner, M. Tignor, S.K. Allen, J. Boschung, A. Nauels, Y. Xia, V. Bex and P.M. Midgley; Cambridge University Press, Cambridge, United Kingdom and New York, NY, USA, p. 741–866. 2013.

Fleming, E.L., Chandra, S., Barnett, J.J., and Corney M.: Zonal mean temperature, pressure, zonal wind, and geopotential height as functions of latitude, COSPAR International Reference Atmosphere: 1986, Part II: Middle Atmosphere Models, Adv. Space Res., 10, 12, 11-59, doi:10.1016/0273-1177(90)90386-E, 1990.

Fox-Kemper, B., Danabasoglu, G., Ferrari, R., Griffies, S. M., Hallberg, R. W., Holland, M., Peacock, S., and Samuels, B.: Parameterization of mixed layer eddies. III: Global implementation and impact on ocean climate simulations. Ocean Modelling 39, 61–78, 2011.

Fox-Kemper, B., Ferrari, R., and Hallberg, R.: Parameterization of mixed layer eddies. I: Theory and diagnosis. Journal of Physical Oceanography, 38, 1145–1165, 2008.

Garcia, R.R., and Richter, J.H.: On the momentum budget of the quasi-biennial oscillation in the whole atmosphere community climate model, J. Atmos. Sci., 76, 69-87, 2019.

Geller, M.A., Zhou, T., Shindell, D., Ruedy, R., Aleinov, I., Nazerenko, L., et al.: Modeling the QBO – Improvements resulting from higher-model vertical resolution, J. Adv. Model. Earth Syst., 8, 1092-1105, 2016.

Good, S.A., Martin, M.J., and Rayner, N.A.: EN4: quality controlled ocean temperature and salinity profiles and monthly objective analyses with uncertainty estimates, Journal of Geophysical Research: Oceans, 118, 6704-6716, doi:10.1002/2013JC009067, 2013.

Griffies, S. M.: Elements of the Modular Ocean Model (MOM), GFDL Ocean Group Technical Report No. 7, NOAA/Geophysical Fluid Dynamics Laboratory, 620pp., 2012.

Griffies, S. M., Gnanadesikan, A., Pacanowski, R. C., Larichev, V., Dukowicz, J. K., and Smith, R. D.: Isoneutral diffusion in a z-coordinate ocean model. Journal of Physical Oceanography 28, 805–830, 1998.

Griffies, S. M., Gnanadesikan, A., Dixon, K. W., Dunne, J. P., Gerdes, R., Harrison, M. J., Rosati, A., Russell, J. L., Samuels, B. L., Spelman, M. J., Winton, M., and Zhang, R.: Formulation of an ocean model for global climate simulations. Ocean Science, 1(1), 45–79, doi:10.5194/os-1-45-2005, 2005.

Haarsma, R. J., Roberts, M. J., Vidale, P. L., Senior, C. A., Bellucci, A., Bao, Q., Chang, P., Corti, S., Fučkar, N. S., Guemas, V., von Hardenberg, J., Hazeleger, W., Kodama, C., Koenigk, T., Leung, L. R., Lu, J., Luo, J.-J., Mao, J., Mizielinski, M. S., Mizuta, R., Nobre, P., Satoh, M., Scoccimarro, E., Semmler, T., Small, J., and von Storch, J.-S.: High Resolution Model Intercomparison Project (HighResMIP v1.0) for CMIP6, Geosci. Model Dev., 9, 4185–4208, doi:10.5194/gmd-9-4185-2016, 2016.

Hack, J. J.: Parameterization of moist convection in the National Center for Atmospheric Research Community Climate Model (CCM2), J. Geophys. Res., 99, 5551-5568, 1994.

Harris, I. C., Jones, P. D., Osborn, T. J., and Lister, D. H.: Updated high-resolution grids of monthly climatic observations – the CRU TS3.10 dataset. Int. J. Climatol., 34, 623–642, doi:10.1002/joc.3711, 2013.

Hwang, Y.-T. and Frierson, D. M. W.: Link between the double-Intertropical Convergence Zone problem and cloud biases over the Southern Ocean, P. Natl. Acad. Sci. USA, 110, 4935–4940, doi:10.1073/pnas.1213302110, 2013.

https://doi.org/10.5194/gmd-2020-284
Preprint. Discussion started: 26 October 2020

Geoscientific Model Development Discussions
Open Access

Hersbach, H., and D. Dee: ERA5 reanalysis is in production. ECMWF Newsletter, No. 147, ECMWF, Reading, United Kingdom, 7, 2016. http://www.ecmwf.int/sites/default/files/elibrary/2016/16299-newsletter-no147-spring-2016.pdf

Hertwig, E., von Storch, J.-S., Handorf, D., Dethloff, K., Fast, I., and Krismer, T.: Effect of horizontal resolution on ECHAM6-AMIP performance, Clim. Dynam., 45, 185–211, doi:10.1007/s00382-014-2396-x, 2015.

Hewitt, H.T., Roberts, M.J., Hyder, P., Graham, T., Rae, J., Belcher, S.E., Bourdallé-Badie, R., Copsey, D., Coward, A., Guiavarch, C., Harris, C., Hill, R., Hirschi, J. J.-M., Madec, G., Mizielinski, M. S., Neininger, E., New, A. L., Rioual, J.-C., Sinha, B., Storkey, D., Shelly, A., Thorpe, L., and Wood, R. A.: The impact of resolving the Rossby radius at mid-latitudes in the ocean: results from a high-resolution version of the Met Office GC2 coupled model. Geosci. Model Dev. 9, 3655–3670, https://doi.org/10.5194/gmd-9-3655-2016, 2016.

Holtslag, A. A. M., and Boville, B. A.: Local versus nonlocal boundary-layer diffusion in a glocal climate model, J. Climate, 6, 1825-1842, 1993.

Huffman, G. J., Bolvin, D. T., Braithwaite, D., Hsu, K., Joyce, R., Kidd, C., Nelkin, E.J., Sorooshian, S., Tan, J., and Xie, P.: NASA Global Precipitation Measurement (GPM) Integrated Multi-satellitE Retrievals for GPM (IMERG), Algorithm Theoretical Basis Document (ATBD) Version 06, 2019.

Ji, J.: A climate-vegetation interaction model: Simulating physical and biological processes at the surface, Journal of Biogeography, 22, 2063-2069, 1995.

Ji, J., Huang, M., and Li, K.: Prediction of carbon exchange between China terrestrial ecosystem and atmosphere in 21st century, Sci. China Ser. D: Earth Sci., 51(6), 885-898, 2008.

Jie, W., Zhang, J., Wu, T., Shi, X., Zhang, F., Li, J., Chu, M., Liu, Q., Yan, J., Ma, Q., Wei, M.: BCC BCC-CSM2HR model output prepared for CMIP6 HighResMIP hist-1950. Version YYYYMMDD[1], Earth System Grid Federation. https://doi.org/10.22033/ESGF/CMIP6.2921, 2020.

Knapp, K. R., Kruk, M. C., Levinson, D. H., Diamond, H. J., and Neumann, C. J.:

The International Best Track Archive for Climate Stewardship (IBTrACS): Unifying Tropical Cyclone Data. Bull. Amer. Meteor. Soc., 91, 363–376, https://doi.org/10.1175/2009BAMS2755.1, 2010.

Kim, H., Caron, J. M., Richter, J. H., and Simpson, I. R.: The lack of QBO‐MJO connection in CMIP6 models. Geophysical Research Letters, 47, e2020GL087295, doi:10.1029/2020GL087295, 2020.

Kinter, J.L., Cash, B., Achuthavarier, D., Adams, J., Altshuler, E., Dirmeyer, P., Doty, B., Huang, B., Jin, E.K., Marx, L., Manganello, J., Stan, C., Wakefield, T., Palmer, T., Hamrud, M., Jung, T., Miller, M., Towers, P., Wedi, N., Satoh, M., Tomita, H., Kodama, C., Nasuno, T., Oouchi, K., Yamada, Y., Taniguchi, H., Andrews, P., Baer, T., Ezell, M., Halloy, C., John, D., Loftis, B., Mohr, R., and Wong, K.: Revolutionizing Climate Modeling with Project Athena: A Multi-Institutional, International Collaboration. Bull. Amer. Meteor. Soc., 94, 231–245, https://doi.org/10.1175/BAMS-D-11-00043.1, 2013.

Klein, S. A. and Hartmann, D. L.: The seasonal cycle of low stratiform cloud, J. Climate, 6, 1587-1606, 1993.

Lal, M., Cubasch, U., Perlwitz, J. P., and Waszkewitz, J.: Simulation of the Indian monsoon climatology in ECHAM3 climate model: Sensitivity to horizontal resolution, Int. J. Climatol., 17, 847–858, 1997.

Large, W., McWilliams, J., and Doney, S.: Oceanic vertical mixing: a review and a model with a nonlocal boundary layer parameterization. Reviews of Geophysics 32, 363–403, 1994.

Li, G., and Xie, S.-P.: Tropical biases in CMIP5 multimodel ensemble: The excessive equatorial Pacific cold tongue and double ITCZ problems, J. Climate, 27, 1765–1780, 2014.

Li, W., Zhang, Y., Shi, X., Zhou, W., Huang, A., Mu, M., Qiu, B., and Ji, J.: Development of the Land Surface Model BCC_AVIM2.0 and Its Preliminary Performance in LS3MIP/CMIP6, J. Meteor. Res., 33, 851–869, https://doi.org/10.1007/s13351-019-9016-y, 2019.

Lu, Y., Wu, T., Jie, W., Scaife, A. A., Andrews, M. B., and Richter, J. H.: Variability

https://doi.org/10.5194/gmd-2020-284
Preprint. Discussion started: 26 October 2020

of the Stratospheric Quasi-Biennial Oscillation and Its Wave Forcing Simulated in the Beijing Climate Center Atmospheric General Circulation Model. J.Atmos.Sci., 77, 149-165, doi:10.1175/JAS-D-19-0123.1, 2020a.

Lu, Y., Wu, T., Li, Y., and Yang, B.: Mitigation of the double ITCZ syndrome in BCC-CSM2-MR through improving parameterizations of boundary-layer turbulence and shallow convection, Geosci. Model Dev. Discuss., https://doi.org/10.5194/gmd-2020-40, in review, 2020b.

Madden, R. A. and Julian, P. R.: Detection of a 40–50 Day Oscillation in the Zonal Wind in the Tropical Pacific, J. Atmos. Sci., 28, 702–708, 1971.

Martin, G. M.: The simulation of the Asian summer monsoon, and its sensitivity to horizontal resolution, in the UK meteorological office unified model, Q. J. Roy. Meteor. Soc., 125, 1499–1525, doi:10.1002/qj.49712555703, 1999.

Manganello, J. V., Hodges, K. I., Kinter, J. L., Cash, B. A., Marx, L., Jung, T., Achuthavarier, D., Adams, J. M., Altshuler, E. L.,Huang, B., Jin, E. K., Stan, C., Towers, P., and Wedi, N.: Tropical Cyclone Climatology in a 10-km Global Atmospheric GCM: Toward Weather-Resolving Climate Modeling, J. Climate, 25, 3867–3893, doi:10.1175/JCLI-D-11-00346.1, 2012.

Manizza, M., Le Quere, C., Watson, A. J., and Buitenhuis, E. T.: Bio-optical feedbacks among phytoplankton, upper ocean physics and sea-ice in a global model. Geophys. Res. Lett., 32, L05603, 2005.

Morel, A., and Antoine, D.: Heating rate within the upper ocean in relation to its bio-optical state, Journal of Physical Oceanography, 24, 1652-1665, 1994.

Masson, S., Terray, P., Madec, G., Luo, J.-J., Yamagata, T., and Takahashi, K.: Impact of intra-daily SST variability on ENSO characteristics in a coupled model, Clim. Dynam., 39, 681–707, 2012.

Masumoto, Y., Sasaki, H., Kagimoto, T., Komori, N., Ishida, A., Sasai, Y., Miyama, T., Motoi, T., Mitsudera, H., Takahashi, K., Sakuma, H., and Yamagata, T.: A fifty-year eddy-resolving simulation of the world ocean – Preliminary outcomes of OFES (OGCM for the Earth Simulator), J. Earth Sim., 1, 35–56, 2004.

McFarlane, N. A.: The effect of orographically excited gravity wave drag on the

https://doi.org/10.5194/gmd-2020-284
Preprint. Discussion started: 26 October 2020

Geoscientific Model Development Discussions

general circulation of the lower stratosphere and troposphere, J. Atmos. Sci., 44, 1775-1800, 1987.

Mizielinski, M. S., Roberts, M. J., Vidale, P. L., Schiemann, R., Demory, M.-E., Strachan, J., Edwards, T., Stephens, A., Lawrence, B. N., Pritchard, M., Chiu, P., Iwi, A., Churchill, J., del Cano Novales, C., Kettleborough, J., Roseblade, W., Selwood, P., Foster, M., Glover, M., and Malcolm, A.: High-resolution global climate modelling: the UPSCALE project, a large-simulation campaign, Geosci. Model Dev., 7, 1629–1640, 2014.

Mizuta, R., Oouchi, K., Yoshimura, H., Noda, A., Katayama, K., Yukimoto, S., Hosaka, M., Kusunoki, S., Kawai, H., and Nakagawa, M.: 20-km-Mesh Global Climate Simulations Using JMAGSMModel: -Mean Climate States-, J. Meteorol. Soc. Jpn., 84, 165–185, 2006.

Murakami, H.: Tropical cyclones in reanalysis data sets. Geophysical Research Letters, 41, 2133-2141, 2014

Murakami, H., Vecchi, G. A., Underwood, S., Delworth, T. L.,Wittenberg, A. T., Anderson,W. G., Chen, J.-H., Gudgel, R. G., Harris, L. M., Lin, S.-J., and Zeng, F.: Simulation and Prediction of Category 4 and 5 Hurricanes in the High-Resolution GFDL HiFLOR Coupled Climate Model, J. Climate, 28, 9058–9079, 2015.

Murakami, H., Wang, Y., Yoshimura, H., Mizuta, R., Sugi, M., Shindo, E., Adachi, Y., Yukimoto, S., Hosaka, M., Kusunoki, S., Ose, T., and Kitoh, A.: Future Changes in Tropical Cyclone Activity Projected by the New High-Resolution MRI-AGCM, J. Climate, 25, 3237–3260, doi:10.1175/JCLI-D-11-00415.1, 2012.

Nicholls, S. and Turton, J. D.: An observational study of the structure of stratiform cloud sheets: Part II. Entrainment. Quart. J. Roy. Meteor. Soc., 112, 461-480, 1986.

Ohfuchi, W., Nakamura, H., Yoshioka, M. K., Enomoto, T., Takaya, K., Peng, X., Yamane, S., Nishimura, T., Kurihara, Y., and Ninomiya, K.: 10-km mesh meso-scale resolving simulations of the global atmosphere on the Earth Simulator: Preliminary outcomes of AFES (AGCM for the Earth Simulator), Journal of the

https://doi.org/10.5194/gmd-2020-284
Preprint. Discussion started: 26 October 2020

Geoscientific Model Development Discussions

Earth Simulator, 1, 8–34, 2004.

Oouchi, K., Yoshimura, J., Yoshimura, H., Mizuta, R., Kusunoki, S., and Noda, A.: Tropical Cyclone Climatology in a Global-Warming Climate as Simulated in a 20 km-Mesh Global Atmospheric Model: Frequency and Wind Intensity Analyses, J. Meteorol. Soc. Japan., 84, 259–276, 2006.

Park, S., and Bretherton, C. S.: The University of Washington shallow convection and moist turbulence schemes and their impact on climate simulations in the Community Atmosphere Model, J. Climate, 22, 3449-3469, 2009.

Peatman, S. C., Matthews, A. J., and Stevens, D. P.: Propagation of the Madden–Julian Oscillation and scale interaction with the diurnal cycle in a high-resolution GCM, Clim. Dynam., 45, 2901–2918, doi:10.1007/s00382-015-2513-5, 2015.

Rackow, T., Goessling, H. F., Jung, T., Sidorenko, D., Semmler, T., Barbi, D., and Handorf, D.: Towards multi-resolution global climate modeling with ECHAM6-FESOM, Part II: climate variability, Clim. Dynam., 1–26, doi:10.1007/s00382-016-3192-6, 2016.

Rasch, P. J., and Kristj´ansson, J. E.: A comparison of the CCM3 model climate using diagnosed and predicted condensate parameterizations, J. Climate, 11, 1587-1614, 1998.

Rayner, N. A., Parker, D. E., Horton, E. B., Folland, C. K., Alexander, L. V., Rowell, D. P., Kent, E. C., and Kaplan, A.: Global analyses of sea surface temperature, sea ice, and night marine air temperature since the late nineteenth century J. Geophys. Res.Vol. 108, No. D14, 4407, doi:10.1029/2002JD002670, 2003.

Reed, K. A., Bacmeister, J. T., Wehner, Rosenbloom, N. A., F., M., Bates, S. C., Lauritzen, P. H., Truesdale, J. T., and Hannay, C.: Impact of the dynamical core on the direct simulation of tropical cyclones in a high-resolution global model, Geophys. Res. Lett.,42, GL063974, doi:10.1002/2015GL063974, 2015.

Richter, I.: Climate model biases in the eastern tropical oceans: Causes, impacts and ways forward. Wiley Interdisciplinary Reviews: Climate Change, 6(3), 345 - 358. doi:10.1002/wcc.338, 2015.

Richter, J.H., Sassi, F., and Garcia, R.R.: Toward a physically based gravity wave

https://doi.org/10.5194/gmd-2020-284
Preprint. Discussion started: 26 October 2020

source parameterization in a general circulation model, J. Atmos. Sci., 67, 136-156, 2010.

Roberts, C. D., Senan, R., Molteni, F., Boussetta, S., Mayer, M., and Keeley, S. P.E.: Climate model configurations of the ECMWF Integrated Forecasting System (ECMWF-IFS cycle 43r1) for HighResMIP, Geosci. Model.Dev., 11, 3681-3721, 2018.

Roberts, M. J., Baker, A., Blockley, E. W., Calvert, D., Coward, A., Hewitt, H. T., Jackson, L. C., Kuhlbrodt, T., Mathiot, P., Roberts, C. D., Schiemann, R., Seddon, J., Vannière, B., and Vidale, P. L.: Description of the resolution hierarchy of the global coupled HadGEM3-GC3.1 model as used in CMIP6 HighResMIP experiments, Geosci. Model Dev., 12, 4999–5028, https://doi.org/10.5194/gmd-12-4999-2019, 2019.

Roberts, M. J., Hewitt, H. T., Hyder, P., Ferreira, D., Josey, S. A., Mizielinski, M., and Shelly, A.: Impact of ocean resolution on coupled air-sea fluxes and large-scale climate. Geophysical Research Letters, 43(19), 10,430-10,438. https://doi.org/10.1002/2016GL070559, 2016.

Sakamoto, T. T., Komuro, Y., Nishimura, T., Ishi, M., Tatebe, H., Shiogama, H., Hasegawa, A., Toyoda, T., Mori, M., Suzuki, T., Imada, Y., Nozawa, T., Takata, K., Mochizuki, T., Ogochi, K., Emori, S., Hasumi, H., and Kimoto, M.: MIROC4h –A New High-Resolution Atmosphere-Ocean Coupled General Circulation Model, J. Meteorol. Soc. Japan, 90, 325–359, 2012.

Sato, T., Miura, H., Satoh, M., Takayabu, Y. N., and Wang, Y. Q.: Diurnal cycle of precipitation in the tropics simulated in a global cloud-resolving model, J. Climate, 22, 4809–4826, 2009.

Satoh, M., Tomita, H., Yashiro, H., Miura, H., Kodama, C., Seiki, T., Noda, A. T., Yamada, Y., Goto, D., Sawada, M., Miyoshi, T., Niwa, Y., Hara, M., Ohno, Y., Iga, S., Arakawa, T., Inoue, T., and Kubokawa, H.: The Non-hydrostatic Icosahedral Atmospheric Model: Description and development, Progress in Earth and Planetary Science, 1, 1, doi:10.1186/s40645-014-0018-1, 2014.

Schenzinger, V., Osprey, S., Gray, L., and Butchart, N.: Defining metrics of the

https://doi.org/10.5194/gmd-2020-284
Preprint. Discussion started: 26 October 2020

Quasi-Biennial Oscillation in global climate models, Geosci. Model Dev., 10, 2157–2168, https://doi.org/10.5194/gmd-10-2157-2017, 2017.

Schiemann, R., Demory, M.-E., Mizielinski, M. S.,and Roberts, M. J., Shaffrey, L. C., Strachan, J., and Vidale, P. L.: The sensitivity of the tropical circulation and Maritime Continent precipitation to climate model resolution, Clim. Dynam., 42, 2455–2468, doi:10.1007/s00382-013-1997-0, 2014.

Shaevitz, D., Camargo, S. J., Sobel, A. H., Jonas, J. A., Kim, D., Kumar, A., LaRow, T. E., Lim, Y.-K., Murakami, H., Reed, K., Roberts, M. J., Scoccimarro, E., Vidale, P. L.,Wang, H.,Wehner, M. F., Zhao, M., and Henderson, N.: Characteristics of tropical cyclones in high-resolution models in the present climate, J. Adv. Model. Earth Syst., 6, 1154–1172, doi:10.1002/2014MS000372, 2014.

Shaffrey, L. C., Stevens, I., Norton, W. A., Roberts, M. J., Vidale, P. L., Harle, J. D., Jrrar, A., Stevens, D. P., Woodage, M. J., Demory, M. E., Donners, J., Clark, D. B., Clayton, A., Cole, J. W., Wilson, S. S., Connolley, W. M., Davies, T. M., Iwi, A. M., Johns, T. C., King, J. C., New, A. L., Slingo, J. M., Slingo, A., Steenman-Clark, L., and Martin, G. M.: UK HiGEM: the new UK High-resolution Global Environment Model – model description and basic evaluation, J. Climate, 22, 1861–1896, doi:10.1175/2008JCLI2508.1, 2009.

Small, R. J., Curchitser, E., Hedstrom, K., Kauffman, B., and Large, W. G.: The Benguela upwelling system: Quantifying the sensitivity to resolution and coastal wind representation in a global climate model, J. Climate, 28, 9409–9432, doi:10.1175/JCLI-D-15-0192.1, 2015.

Small, R. J., Bacmeister, J., Bailey, D. A., Baker, A., Bishop, S., Bryan, F. O., Caron, J., Dennis, J., Gent, P. R., Hsu, H.-M., Jochum, M., Lawrence, D. M., Munoz Acevedo, E., diNezio, P., Scheitlin, T., Tomas, R., Tribbia, J., Tseng, Y., and Vertenstein, M.: A new synoptic scale resolving global climate simulation using the Community Earth System Model. J. Adv.Model. Earth Syst., 6, 1065–1094, https://doi.org/10.1002/2014MS000363, 2014.

Smith, R. D., Maltrud, M. E., Bryan, F. O., and Hecht, M. W.: Numerical Simulation of the North Atlantic Ocean at 1/10°, J. Phys. Oceanogr., 30, 1532–1561, 2000.

Sperber, K. R., Sultan, H., Potter, G. L., and Boyle, J. S.: Simulation of the Northern summer monsoon in the ECMWF model: sensitivity to horizontal resolution, Mon. Weather Rev., 122, 2461–2481, 1994.

Stevens, B., Fiedler, S., Kinne, S., Peters, K., Rast, S., Müsse, J., Smith, S. J., and Mauritsen, T.: MACv2-SP: a parameterization of anthropogenic aerosol optical properties and an associated Twomey effect for use in CMIP6, Geosci. Model Dev., 10, 433–452, doi:10.5194/gmd-10-433-2017, 2017.

Strachan, J., Vidale, P. L., Hodges, K., Roberts, M., and Demory, M.-E.: Investigating global tropical cyclone activity with a hierarchy of AGCMs: The role of model resolution, J. Clim., 26, 133–152, 2013.

Sweby, P. K.: High resolution schemes using flux limiters for hyperbolic conservation laws, SIAM Journal on Numerical Analysis, 21(5), 995-1011, 1984.

Taylor, K. E., Stouffer, R. J., and Meehl, G. A.: An Overview of Cmip5 and the Experiment Design, B. Am. Meteorol. Soc., 93, 485–498, 2012.

Tian, B., Fetzer, E.J., Kahn, B.H., Teixeira, J., Manning, E., and Hearty, T.: Evaluating CMIP5 models using AIRS tropospheric air temperature and specific humidity climatology. J Geophys Res Atmos 118:114–134. doi:10.1029/2012JD018607, 2013.

Turton, J. D., and Nicholls, L.: A study of the diurnal variation of stratocumulus using a multiple mixed-layer model, Q. J. R. Meteorol. Soc., 113, 969-1009, 1987.

Vellinga, M., Roberts, M., Vidale, P. L., Mizielinski, M., Demory, M.-E., Schiemann, R., Strachan, J., Bain, C., Kettleborough, J., Good, P., Edmond, I., and Hibling, E.: Organised convection as the main carrier of Sahel rainfall variability at multi-annual timescales, Geophys. Res. Lett., 43, 326–333, doi:10.1002/2015GL066690, 2016.

Walsh, K., Lavender, S., Scoccimarro, E., and Murakami, H.: Resolution dependence of tropical cyclone formation in CMIP3 and finer resolution models, Clim. Dynam., 40, 585–599, 2012.

Wehner, M. F., Smith, R. L., Bala, G., and Duffy, P.: The effect of horizontal resolution on simulation of very extreme US precipitation events in a global atmosphere model. Clim. Dyn., 34, 241–247, 2010.

Wehner, M. F., Prabhat, Reed, K. A., Stone, D., Collins, W. D., and Bacmeister, J. T.: Resolution dependence of future tropical cyclone projections of CAM5.1 in the US CLIVAR Hurricane Working Group idealized configurations, J. Climate, 28, 3905–3925, doi:10.1175/JCLI-D-14-00311.1, 2015.

Wheeler, M. C., and Hendon, H. H.: An all-season real-time multivariate MJO index: Development of an index for monitoring and prediction, Mon. Weather Rev., 132, 1917–1932, 2004.

Wheeler, M., and Kiladis, G. N.: Convectively coupled equatorial waves: Analysis of clouds and temperature in the wavenumber-frequency domain, J. Atmos. Sci., 56, 374– 399, 1999.

Whitehead, J. P., Jablonowski, C., Rood, R. B., and Lauritzen, P.H.: A stability analysis of divergence damping on a latitude–longitude grid. Mon. Wea. Rev., 139, 2976–2993, 2011.

Wielicki, B.A., Barkstrom, B. R., Harrison, E. F., Lee, R. B., Smith, G. L., and Cooper, J. E.: Clouds and the earth's radiant energy system (CERES): an earth observing system experiment, Bull. Am. Meteorol. Soc., 77, 853–868, 1996.

Wood, R. and Bretherton, C. S.: Boundary-layer depth, entrainment, and decoupling in the cloud-capped subtropical and tropical marine boundary layer, J. Climate, 17, 3576-3588, 2004.

Wu, T., Song, L., Li, W., Wang, Z., Zhang, H., Xin, X., Zhang, Y., Zhang, L., Li, J., Wu, F., Liu, Y., Zhang, F., Shi, X., Chu, M., Zhang, J., Fang, Y., Wang, F., Lu, Y., Liu, X., Wei, M., Liu, Q., Zhou, W., Dong, M., Zhao, Q., Ji, J., Li, L., and Zhou, M.: An overview of BCC climate system model development and application for climate change studies. J. Meteor. Res., 28(1), 34-56, 2014.

Wu, T., Li, W., Ji, J., Xin, X., Li, L., Wang, Z, Zhang, Y., Li, J., Zhang, F., Wei, M., Shi, X., Wu, F., Zhang, L., Chu, M., Jie, W., Liu, Y., Wang, F., Liu, X., Li, Q., Dong, M., Liang, X., Gao, Y., and Zhang, J.: Global carbon budgets simulated by the Beijing climate center climate system model for the last century. J Geophys

https://doi.org/10.5194/gmd-2020-284
Preprint. Discussion started: 26 October 2020

Geoscientific Model Development Discussions

Res Atmos, 118, 4326-4347. doi: 10.1002/jgrd.50320, 2013.

Wu, T., Yu, R., Zhang, F., Wang, Z., Dong, M., Wang, L., Jin, X., Chen, D., and Li, L.: The Beijing Climate Center atmospheric general circulation model: description and its performance for the present-day climate, Climate Dynamics, 34, 123-147, doi:10.1007/s00382-008-0487-2, 2010.

Wu, T., Lu, Y., Fang, Y., Xin, X., Li, L., Li, W., Jie, W., Zhang, J., Liu, Y., Zhang, L., Zhang, F., Zhang, Y., Wu, F., Li, J., Chu, M., Wang, Z., Shi, X., Liu, X., Wei, M., Huang, A., Zhang, Y., and Liu, X.: The Beijing Climate Center Climate System Model (BCC-CSM): Main Progress from CMIP5 to CMIP6, Geosci. Model Dev., 12, 1573–1600, 2019.

Wu, T., Zhang, F., Zhang, J., Jie, W., Zhang, Y., Wu, F., Li, L., Yan, J., Liu, X., Lu, X., Tan, H., Zhang, L., Wang, J., and Hu, A.: Beijing Climate Center Earth System Model version 1 (BCC-ESM1): model description and evaluation of aerosol simulations, Geosci. Model Dev., 13, 977–1005, doi:10.5194/gmd-13-977-2020, 2020a.

Wu, T., Yu, R., Lu, Y., Jie, W., et al.: Source code for Wu et al, "BCC-CSM2-HR: A High-Resolution Version of the Beijing Climate Center Climate System Model", GMD publication. http://doi.org/10.5281/zenodo.4127457, 2020b.

Wu, T., Yu, R., and Zhang, F.: A modified dynamic framework for atmospheric spectral model and its application, J. Atmos.Sci., 65, 2235-2253, 2008.

Wu, T.: A Mass-Flux Cumulus Parameterization Scheme for Large-sistercale Models: Description and Test with Observations, Clim. Dyn., 38, 725–744, doi:10.1007/ s00382-011-0995-3, 2012.

Xin, X., Wu, T., and Zhang, J.: Introduction of CMIP5 experiments carried out with the climate system models of Beijing Climate Center. Adv. Clim. Change Res., 4(1), 41-49, doi: 10.3724/SP.J.1248.2013.041, 2013.

Xin, X., Wu, T., Zhang, J., Zhang, F., Li, W., Zhang, Y., Lu, Y., Fang, Y., Jie, W., Zhang, L., Dong, M., Shi, X., Chu, M., Liu Q., and Yan, J.: Introduction of BCC models and its participation in CMIP6, Climate Change Research, 15 (5): 533-539, https://doi.org/10.12006/j.issn.1673-1719.2019.039, 2019.

https://doi.org/10.5194/gmd-2020-284
Preprint. Discussion started: 26 October 2020

Yamada, Y., Satoh, M., Sugi, M., Kodama, C., Noda, A. T., Nakano, M., and Nasuno, T.: Response of tropical cyclone activity and structure to global warming in a high-resolution global nonhydrostatic model. Journal of Climate, 30, 9703– 9724, 2017.

Yu, R., Zhou, T., Wu, T., Xue, W., and Zhou, G.: Development and Evaluation of High Resolution Climate System Models, Springer, 258pp, doi:10.1007/978-981-10-0033-1, 2016.

Zarzycki, C. M., Reed, K. A., Bacmeister, J. T., Craig, A. P., Bates, S. C., and Rosenbloom, N. A.: Impact of surface coupling grids on tropical cyclone extremes in high-resolution atmospheric simulations, Geos. Model Dev., 9, 779-788, 2016.

Zhang, M., Lin, W., Bretherton, C. S., Hack, J. J., and Rasch, P. J.: A modified formulation of fractional stratiform condensation rate in the NCAR community atmospheric model CAM2, J. Geophys. Res., 108 (D1), 2003.

Zhang, Y., Gao, Z., Li, D., Li, Y., Zhang, N., Zhao, X., and Chen, J.: On the computation of planetary boundary-layer height using the bulk Richardson number method, Geosci. Model Dev., 7, 2599–2611, 2014.

Zhao, M., Held, I. M., and Lin, S.-J.: Some counterintuitive dependencies of tropical cyclone frequency on parameters in a GCM, J. Atmos. Sci., 69, 2272-2283, 2012.

Zhao, M., Held, I. M., Lin, S. J., and Vecchi, G. A.: Simulations of Global Hurricane Climatology, Interannual Variability, and Response to Global Warming Using a 50 km Resolution GCM, J.Climate, 33, 6653–6678, 2009.

https://doi.org/10.5194/gmd-2020-284
Preprint. Discussion started: 26 October 2020

Geoscientific Model Development Discussions
Open Access EGU

Table 1. Constituents and configurations of BCC-CSM2-MR and BCC-CSM2-HR.

		BCC-CSM2-MR	**BCC-CSM2-HR**
Atmosphere component (BCC-AGCM)	**Resolution**	T106 (~110km), 46 layers with top layer at 1.979hPa and model lid at 1.459 hPa	T266 (~45km), 56 layers with top layer at 0.156 hPa and model lid at 0.092 hPa
	Dynamic core	Spectral framework described in Wu et al. (2008)	Same as in BCC-CSM2-MR but including spatially variant divergence damping.
	Deep convection	A modified Wu'2012 scheme described in Wu et al. (2019)	Revised Wu et al. (2019) scheme, including the effects of convective downdraft in neighboring grids.
	Shallow/Middle Tropospheric Moist Convection	Hack (1994)	Modified Hack (1994) scheme described in Lu et al. (2020b), incorporating a trigger based on lower tropospheric stability.
	Cloud macrophysics	Diagnosed cloud fraction described in Wu et al. (2019)	Revised Wu et al. (2019) scheme, excluding the special treatment for the marine stratocumulus.
	Cloud microphysics	Modified scheme of Rasch and Kristj´ansson (1998) by Zhang et al. (2003), but included the aerosol indirect effects in which liquid cloud droplet number concentration is diagnosed using the aerosols masses.	Same as in BCC-CSM2-MR.
	Gravity wave drag	Gravity wave drag generated by both orography (Mcfarlane 1987) and convection (Beres et al., 2004).	Same as in BCC-CSM2-MR, but using tuned parameters related to model resolutions.
	Surface orographic drag	No treatment.	The turbulent mountain stress scheme as in Richter et al. (2010).
	Radiative transfer	Radiative transfer scheme used in CAM3 (Collins et al., 2004), but including the aerosol indirect effects, and the effective radius of the cloud droplet for liquid clouds is diagnosed using liquid cloud droplet number concentration.	Same as in BCC-CSM2-MR.
	Boundary Layer	Parameterization of Holtslag and Boville (1993), but modified PBL height computation as in Zhang et al. (2014)	The University of Washington Moist Turbulence scheme (Bretherton and Park, 2009)
Land surface component (BCC-AVIM)	**Resolution**	Horizontal resolution same as in the atmosphere component. 10 layers for soil and up to five layers for snow.	Horizontal resolution same as in the atmosphere component. 10 layers for soil and up to five layers for snow.
	Biophysical process	CLM3	CLM3
	Plant physiological and Soil carbon-nitrogen dynamical processes	BCC-AVIM2 (Li et al., 2019)	BCC-AVIM2 (Li, 2019)
Ocean Component (MOM)	**Resolution**	1°×1° with a tri-pole grid, but 1/3° latitude between 30°S and 30°N to 1.0° at 60° latitude, 40 layers in vertical	1/4°×1/4° with a tri-pole grid at north to 60°N, 50 layers in vertical
	Tracer advection scheme	MOM4 (Griffies, 2005), Sweby advection scheme (Sweby, 1984)	MOM5 (Griffies, 2012), multi-dimensional piecewise parabolic method
	Neutral diffusion scheme	Griffies et al. (1998) with a constant diffusivity of 600 $m^2 s^{-1}$	None
	Surface boundary layer processes	K-profile parameterization (KPP, Large et al., 1994)	Same as in MOM4
	Submesoscale parameterization	None	Fox-Kemper et al. (2008)

	scheme		
	shortwave penetration	Morel and Antoine (1994), with the maximum depth of 100m	Manizza et al. (2005), with the maximum depth of 300m
Sea Ice Component (SIS)	**Resolution**	Same as in the ocean component, 3 vertical layers including 1 snow cover and 2 ice layers of equal thickness	Same as in the ocean component, 3 vertical layers including 1 snow cover and 2 ice layers of equal thickness
	Model physics	SISv1, Elastic-viscous-plastic dynamic processes, Semtner's thermodynamic processes	Same as SISv2
	Snow albedo	0.80	0.85
	Ice albedo	0.5826	0.68

https://doi.org/10.5194/gmd-2020-284
Preprint. Discussion started: 26 October 2020

Geoscientific Model Development Discussions
Open Access
EGU

Table 2. Energy balance and cloud radiative forcing at the top-of-atmosphere (TOA) in the models with contrast to CERES-EBAF observations. Units: $W \cdot m^{-2}$.

	BCC-CSM2-MR	**BCC-CSM2-HR**	**CERES-EBAF**
Net energy at TOA	1.81 ± 0.49	1.08 ± 0.46	0.84 ± 0.33
TOA outgoing longwave radiative flux	239.13 ± 0.29	238.52 ± 0.35	239.69 ± 0.25
TOA net shortwave radiative flux	240.95 ± 0.55	239.60 ± 0.45	240.53 ± 0.19
TOA outgoing longwave radiative flux in clear sky	265.05 ± 0.41	266.12 ± 0.46	265.67 ± 0.37
TOA net shortwave radiative flux in clear sky	290.52 ± 0.85	289.77 ± 0.70	287.68 ± 0.14
TOA incoming shortwave radiation	340.38 ± 0.09	340.38 ± 0.09	340.14 ± 0.09
Shortwave cloud radiative forcing	-49.58 ± 0.49	-50.17 ± 0.58	-47.16 ± 0.24
Longwave cloud radiative forcing	25.92 ± 0.19	27.60 ± 0.19	25.99 ± 0.25

Notes: Mean value and standard deviation are calculated from yearly global means of the 1971-2000 simulations for BCC-CSM2-MR, BCC-CSM2-HR, and the 2001-2014 CERES-EBAF Ed2.8 data set.

https://doi.org/10.5194/gmd-2020-284
Preprint. Discussion started: 26 October 2020

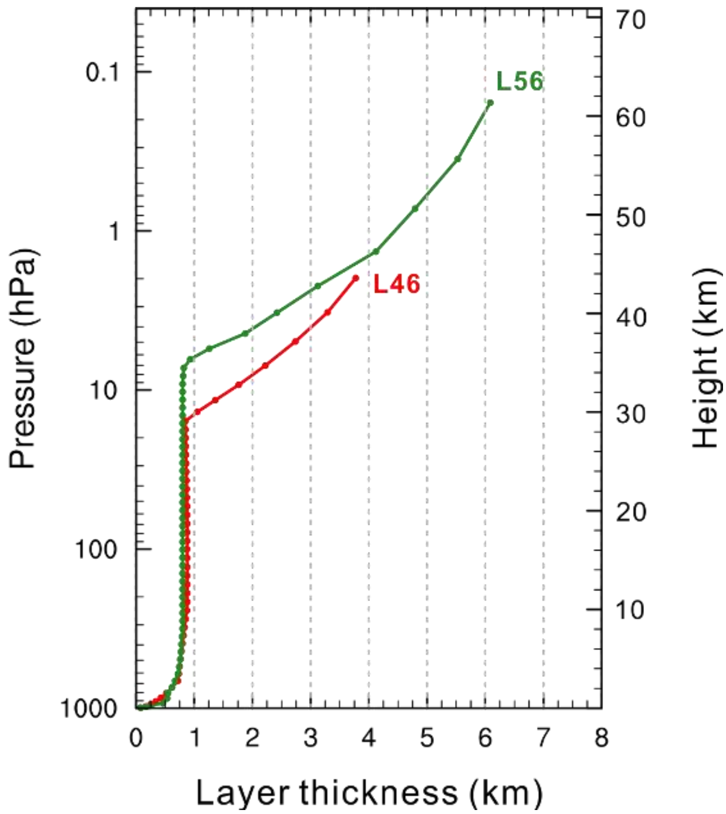

Figure 1. The profiles of layer thickness against height for 46 vertical layers in BCC-CSM2-MR (red) and 56 vertical layers in BCC-CSM2-HR (green).

https://doi.org/10.5194/gmd-2020-284
Preprint. Discussion started: 26 October 2020

Geoscientific Model Development
Discussions
Open Access

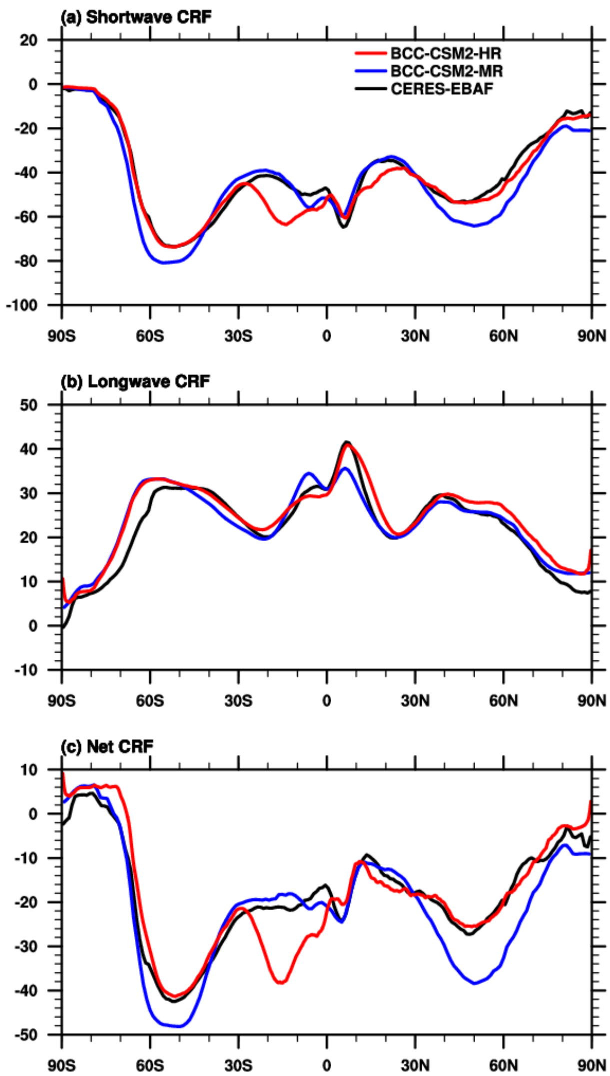

Figure 2. Zonal averages of the cloud radiative forcing (CRF, in W m^{-2}) for the historical simulations (1971-2000) of BCC-CSM2-MR and BCC-CSM2-HR, compared to the CERES-EBAF observations (2001-2014, a: shortwave effect; b: longwave effect; c: net effect).

https://doi.org/10.5194/gmd-2020-284
Preprint. Discussion started: 26 October 2020

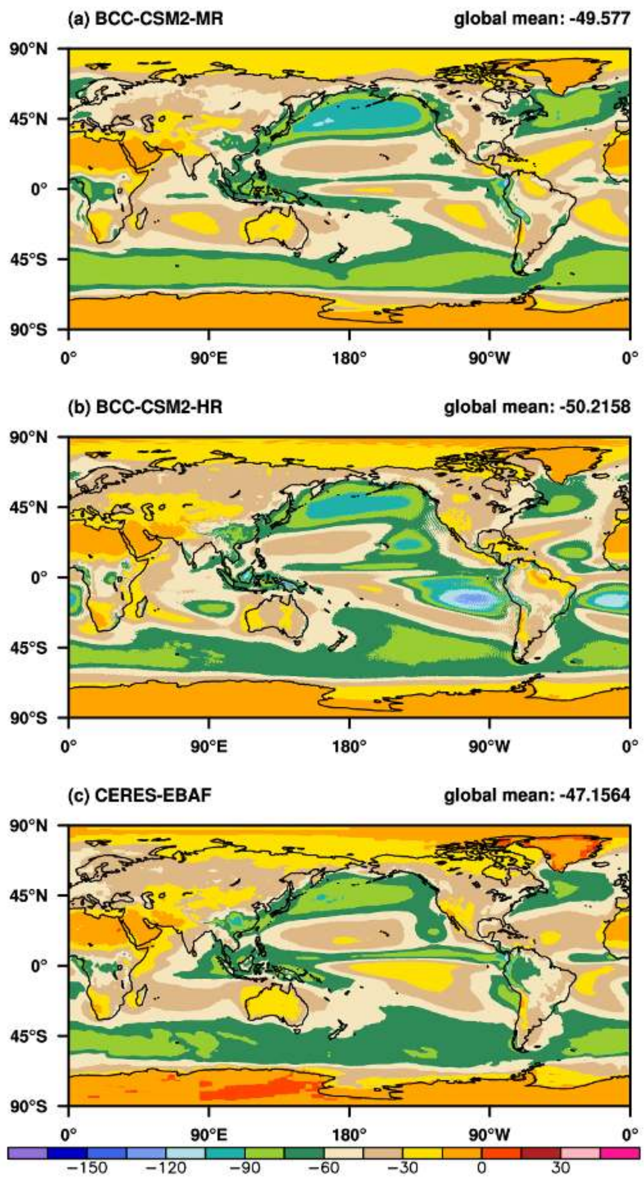

Figure 3. Annual-mean shortwave cloud radiative forcing for the historical simulations (1971 to 2000) of (a) BCC-CSM2-MR and (b) BCC-CSM2-HR, with comparison against (c) the CERES-EBAF observations (2001-2014). Units: W·m^{-2}.

Geoscientific Model Development
Discussions

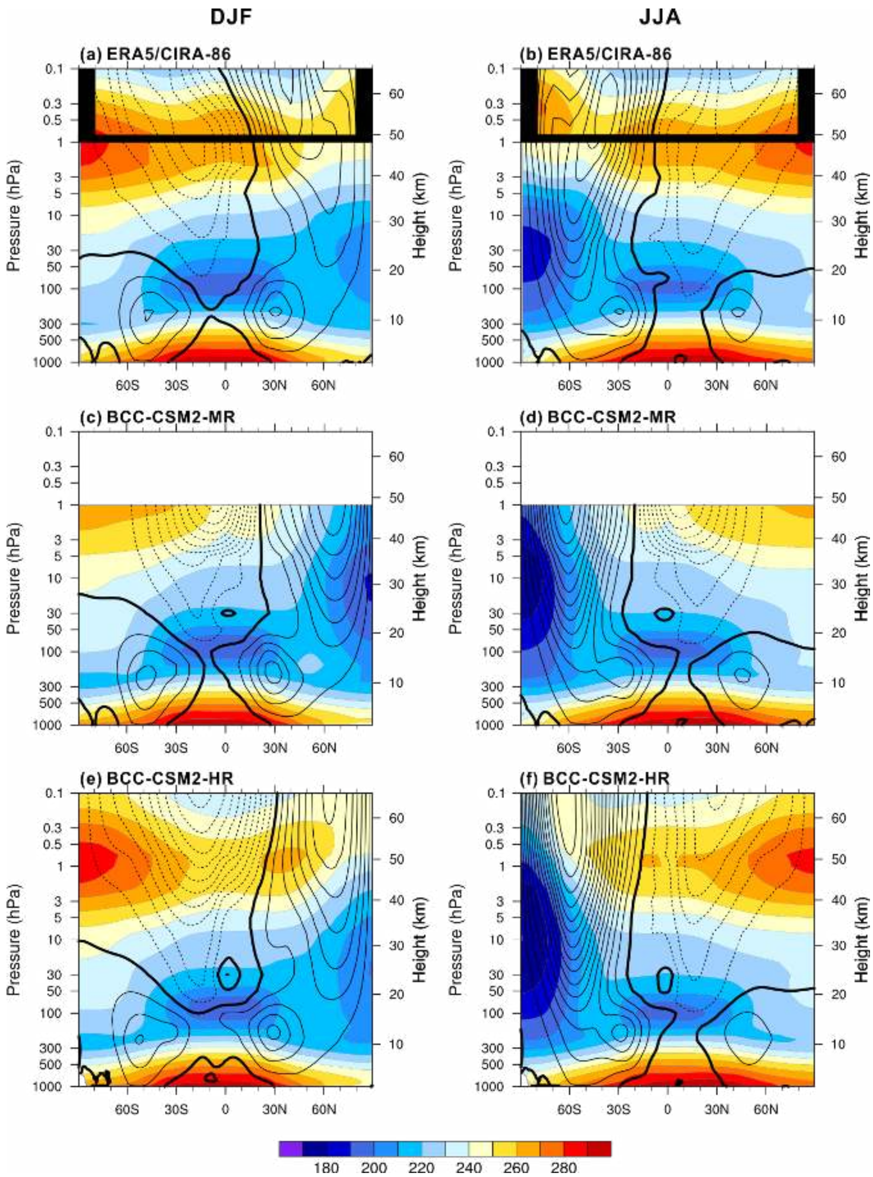

Figure 4. The zonal means of temperature (colors; K) and zonal wind (contours; m s^{-1}) averaged for December-January-February (left panel) and Jun-July-August (right panel) from 1971 to 2000 for (a,b) ERA5/CIRA86, (c,d) BCC-CSM2-MR, (e,f) BCC-CSM2-HR. Positive (negative) zonal winds are plotted with solid (dashed) lines with a contour interval of 10 m s^{-1}. Thick contour line denotes zero zonal wind speed. In (a) and (b), the values above 1 hPa from the COSPAR International Reference Atmosphere (CIRA86, Fleming et al., 1990) and below 1 hPa from the ERA5 reanalysis.

https://doi.org/10.5194/gmd-2020-284
Preprint. Discussion started: 26 October 2020

1274

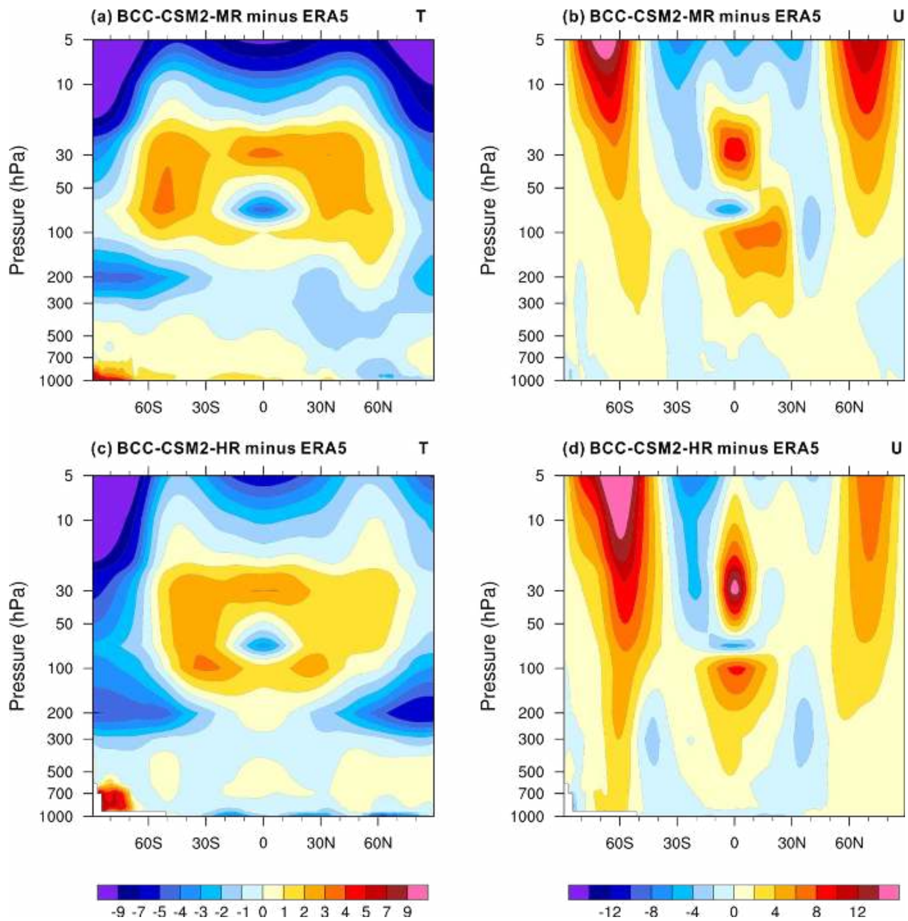

1275

1276

1277

1278 Figure 5. Zonally-averaged annual mean temperature biases (left panel, in K) and zonal wind
1279 biases (right panel, in m·s^{-1}) averaged for the period from 1971 to 2000 for (a,b)
1280 BCC-CSM2-MR, and (c,d) BCC-CSM2-HR, with respect to the ERA5 reanalysis data.

1281

https://doi.org/10.5194/gmd-2020-284
Preprint. Discussion started: 26 October 2020

Geoscientific Model Development
Discussions

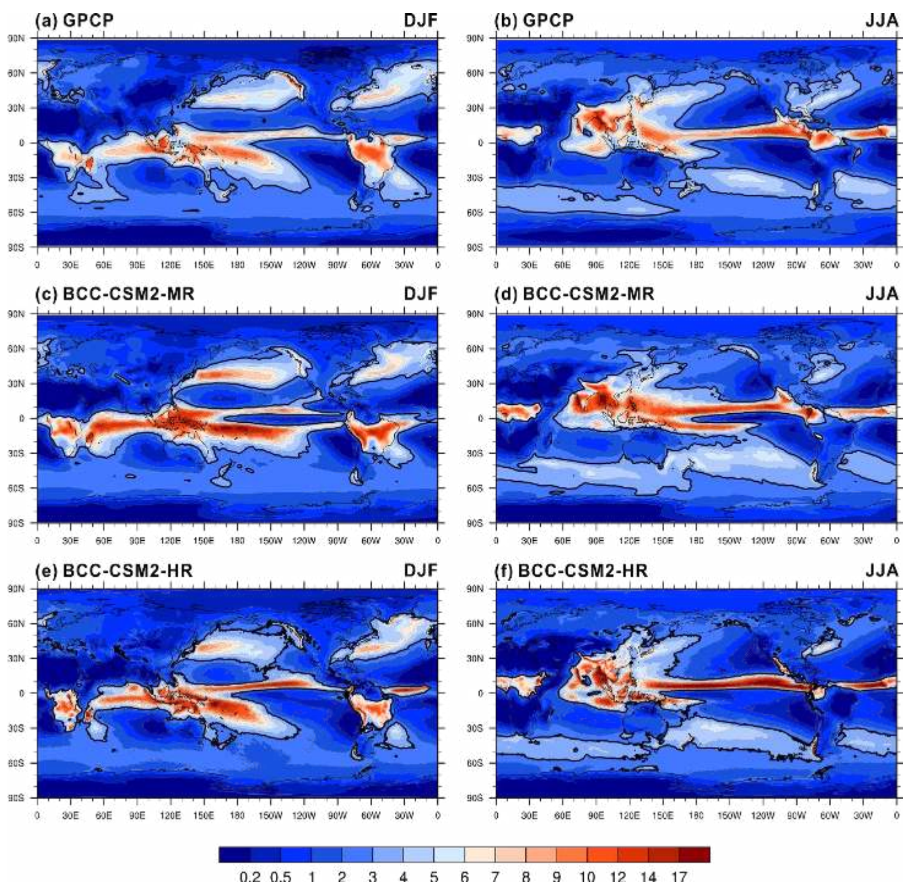

Figure 6. The mean precipitation rate of December-January-February (left panel) and June-July-August (right panel) for (a,b) GPCP observations (1981−2010), (c,d) BCC-CSM2-MR (1971−2000), and (e,f) BCC-CSM2-HR (1971−2000). Units: mm·day^{-1}. The 3 mm·day^{-1} contour line is in bold as a reference to facilitate the visual inspection.

Geoscientific Model Development
Discussions
Open Access

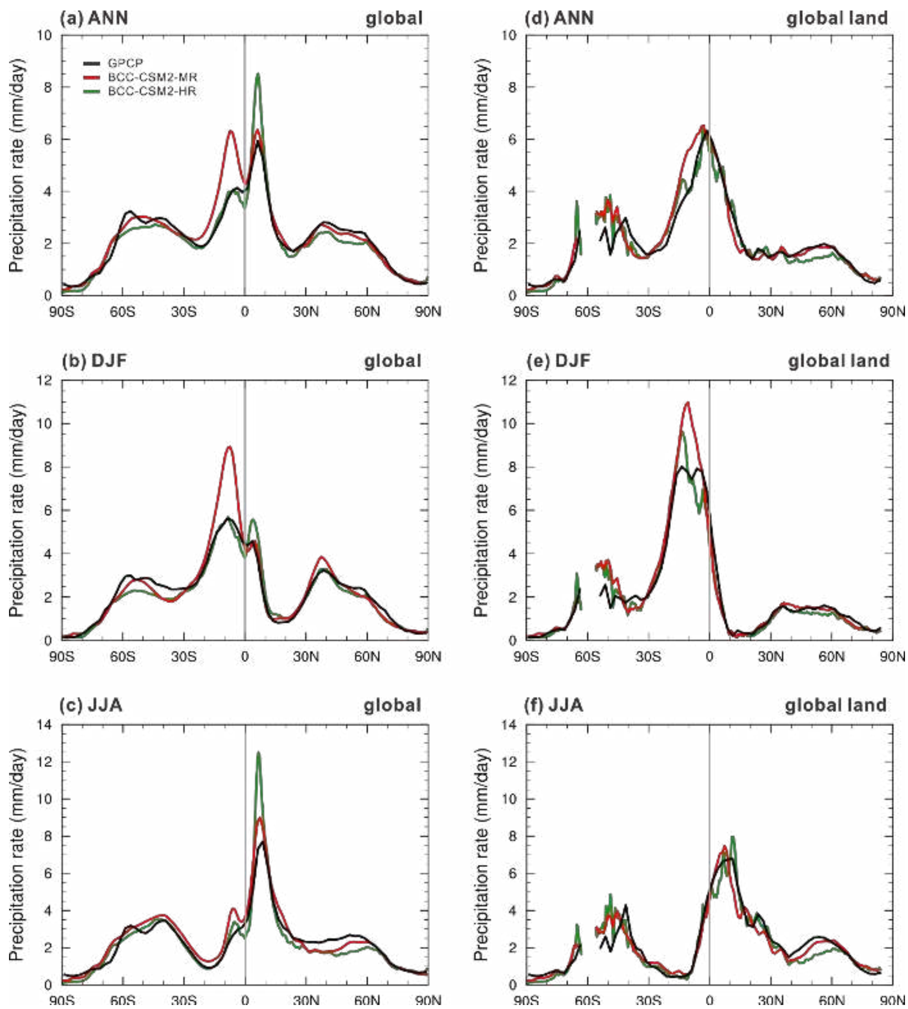

Figure 7. The zonally-averaged mean precipitation rate (mm day^{-1}) averaged for (a, d) the annual mean, (b, e) December-February-February, and (c, f) June-July-August. The solid black lines denote GPCP data (1981–2010), and the color lines show BCC-CSM2-MR (1971–2000) and BCC-CSM2-HR (1971–2000) simulations. Units: mm·day^{-1}.

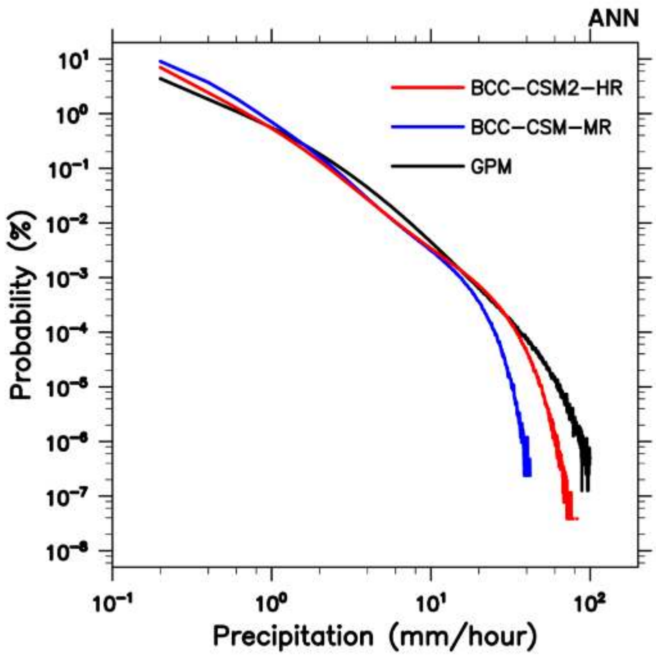

Figure 8. The probability density of hourly precipitation in function of precipitation intensity with intervals of 1 mm/hour between 40°S and 40°N derived from every 3 hours data for the Global Precipitation Measurement (GPM) from 2001 to 2019, and for BCC-CSM2-MR and BCC-CSM2-HR simulations from 1971 to 2000.

https://doi.org/10.5194/gmd-2020-284
Preprint. Discussion started: 26 October 2020

Geoscientific Model Development Discussions

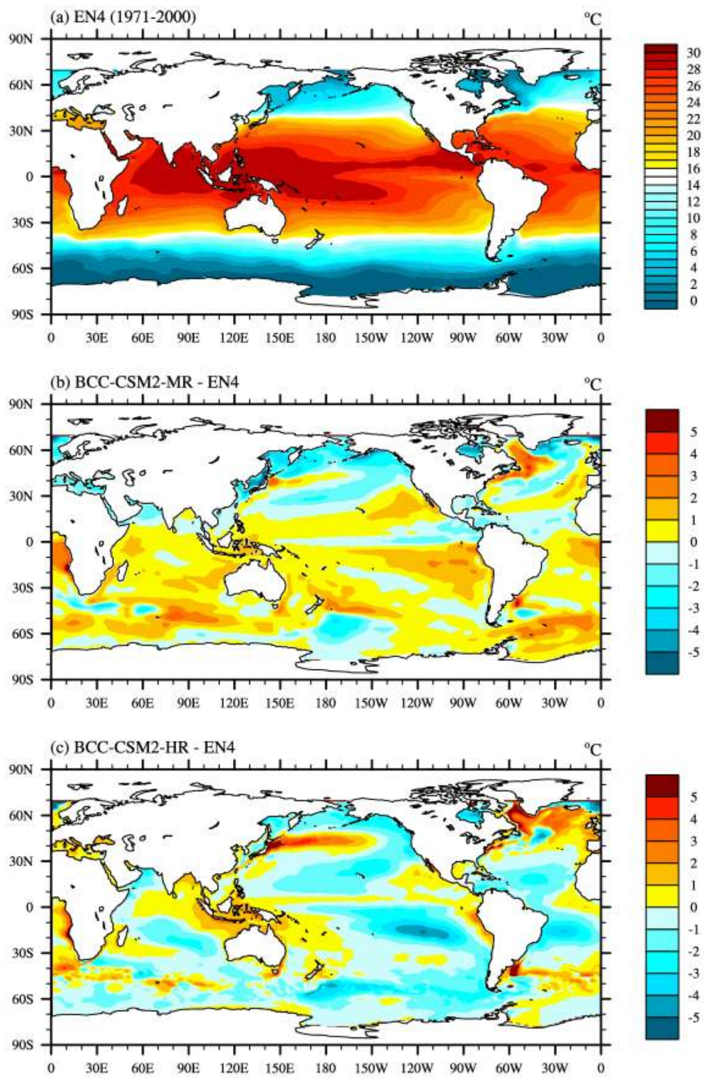

Figure 9. The global distributions of the 1971-2000 annual mean sea surface temperature for (a) the observations from Met Office Hadley Centre EN4 dataset, and the simulation biases in (b) BCC-CSM2-MR and (c) BCC-CSM2-HR.

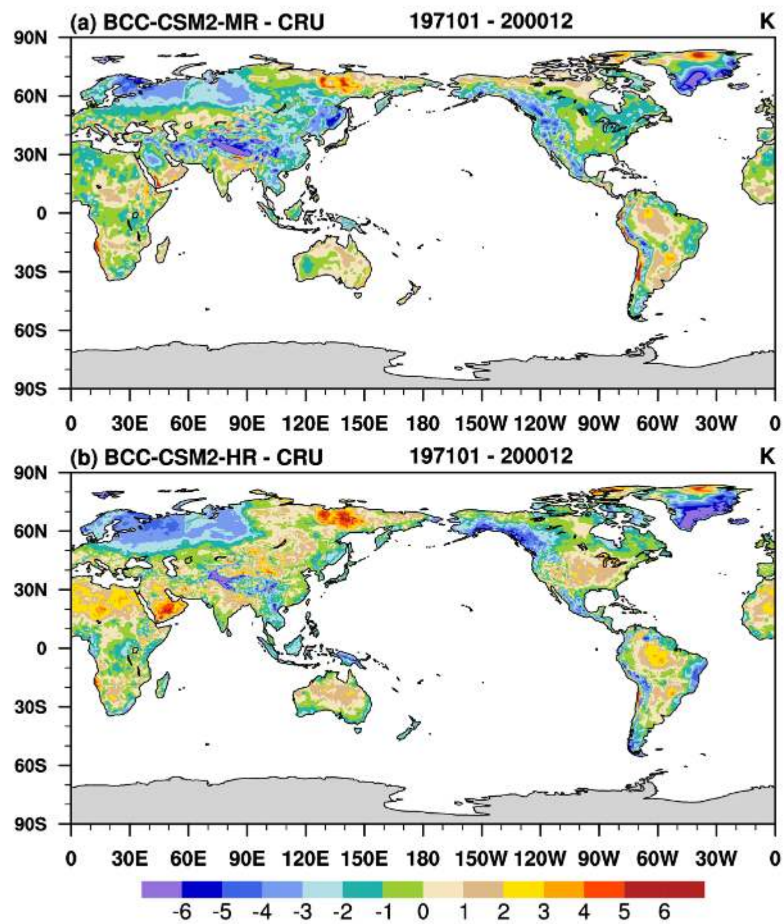

Figure 10. The simulation biases of annual mean land-surface air temperature in BCC-CSM2-MR and BCC-CSM2-HR, with contrast to HadCRUT global land-surface air temperature observations during the period from 1971 to 2000.

Geoscientific Model Development Discussions
Open Access

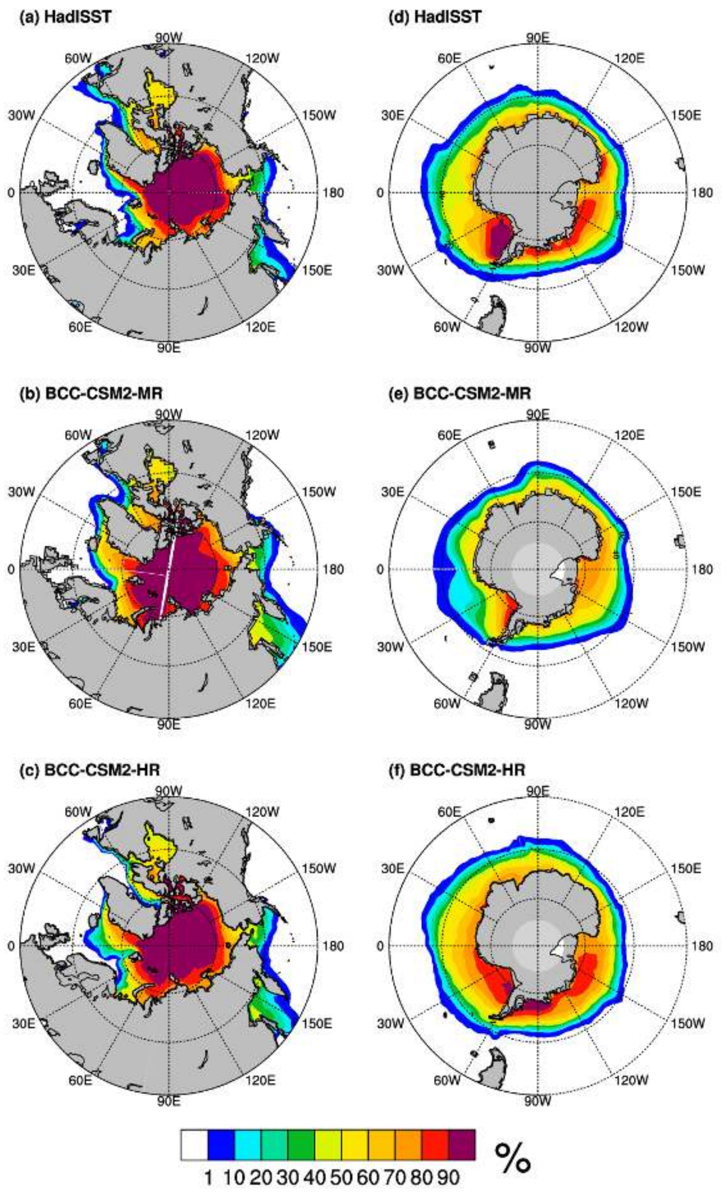

Figure 11. The annual mean sea ice extents from BCC-CSM2-MR and BCC-CSM2-HR with contrast to the observations from the Hadley Centre Sea Ice data set from 1971 to 2000.

https://doi.org/10.5194/gmd-2020-284
Preprint. Discussion started: 26 October 2020

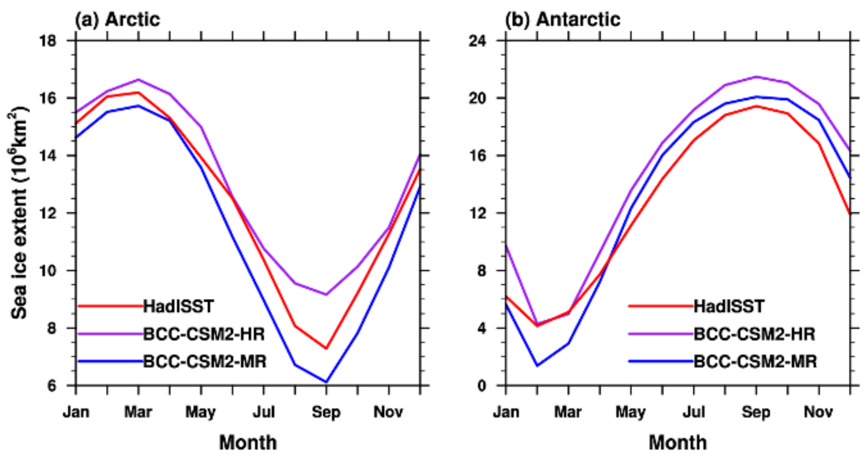

Figure 12. The mean (1971-1990) seasonal cycle of sea-ice extent (with a sea-ice concentration of at least 15 %) in (a) the Northern Hemisphere and (b) the Southern Hemisphere for the observations from the Hadley Centre Sea Ice and Sea Surface Temperature data set (red lines) and the simulations from BCC-CSM2-MR (blue lines), BCC-CSM2-HR (purple line).

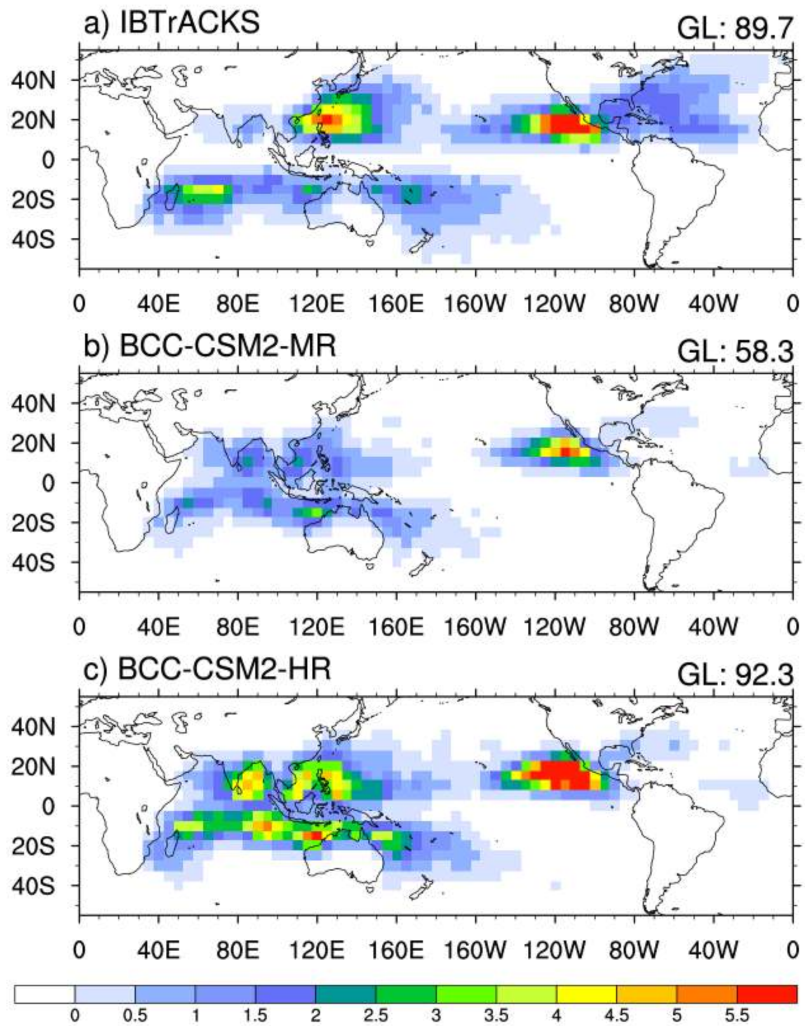

Figure 13. The global distribution of tropical cyclone (TC) densities (number per year) averaged for (a) the 1981-2000 IBTrACS_wmo observations and the 1981-2000 simulations from (b) BCC-CSM2-MR, and (c) BCC-CSM2-HR. The value on the upper-right corner denotes the total number of global TCs on 5°×5° grid box.

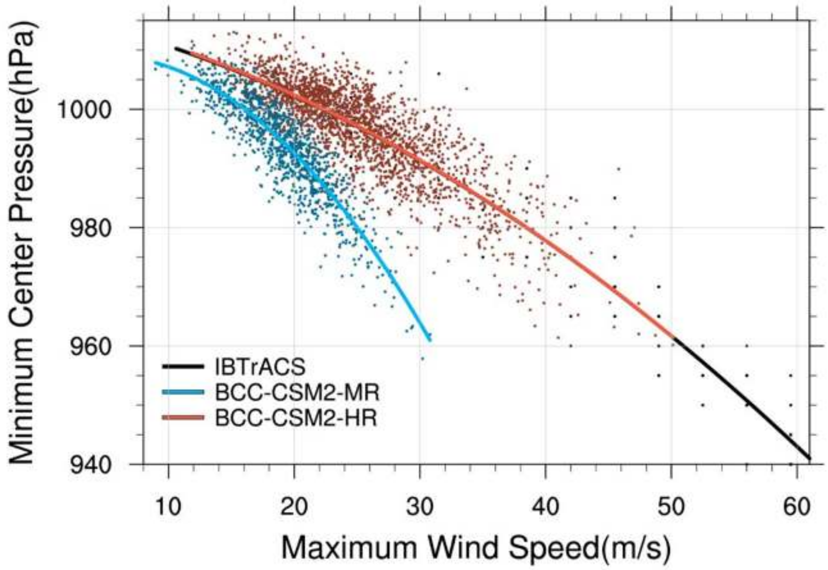

Figure 14. Maximum surface wind speed (m s^{-1}) versus minimum sea level pressure (hPa) for tropical cyclones from the 1981-2000 daily IBTrACS observation (black dots and fitting line), and the 1981-2000 daily simulation from BCC-CSM2-HR (red dots and fitting line) and BCC-CSM2-MR (blue dots and fitting line). Here only plotted the tropical cyclones whose maximum surface wind speed exceeds 10 m s^{-1}.

https://doi.org/10.5194/gmd-2020-284
Preprint. Discussion started: 26 October 2020

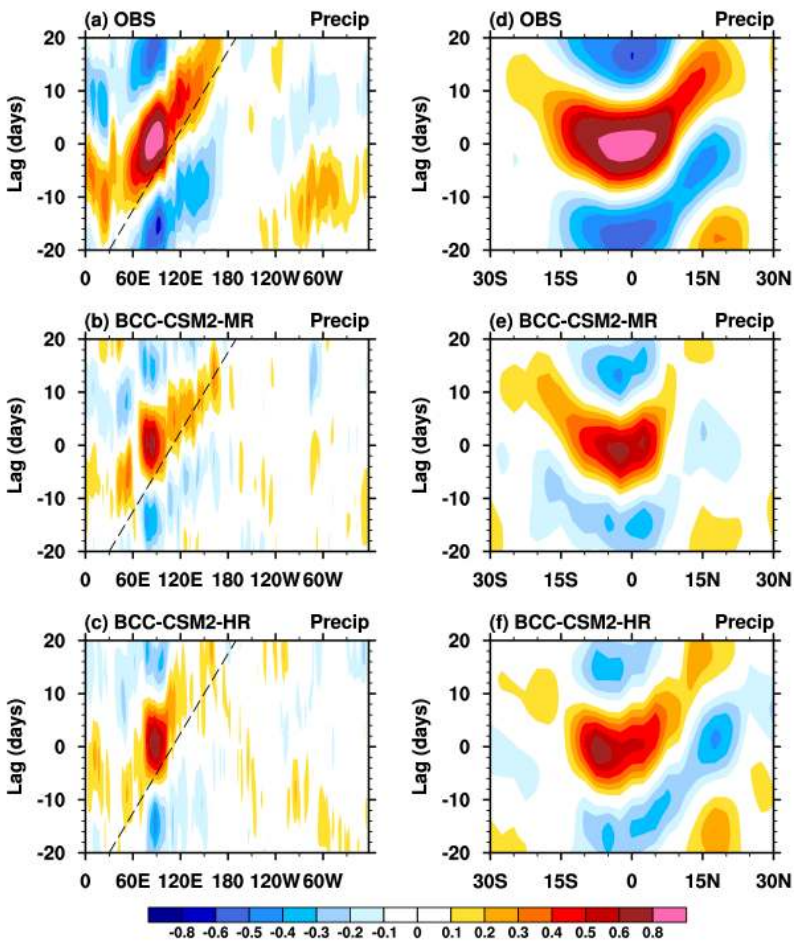

Figure 15. Left panels: longitude-time evolution of lagged correlation coefficient for the 20–100-day band-pass-filtered precipitation anomaly (averaged over 10°S–10°N) against regional averaged precipitation over the equatorial eastern Indian Ocean (80°–100°E, 10°S–10°N). Right panels: same as the left panels, but for the latitude-time evolution of lagged correlation coefficient for filtered precipitation anomaly (averaged over 80°–100°E) against the regional averaged precipitation over the equatorial eastern Indian Ocean. Dashed lines in each panel denote the 5 $m \cdot s^{-1}$ eastward propagation speed. The observations in (a, b) are derived from GPCP data and the simulations are from (c,d) BCC-CSM2-MR, and (e,f) BCC-CSM2-HR for the period from 1971-2000.

https://doi.org/10.5194/gmd-2020-284
Preprint. Discussion started: 26 October 2020

Geoscientific Model Development Discussions
Open Access
EGU

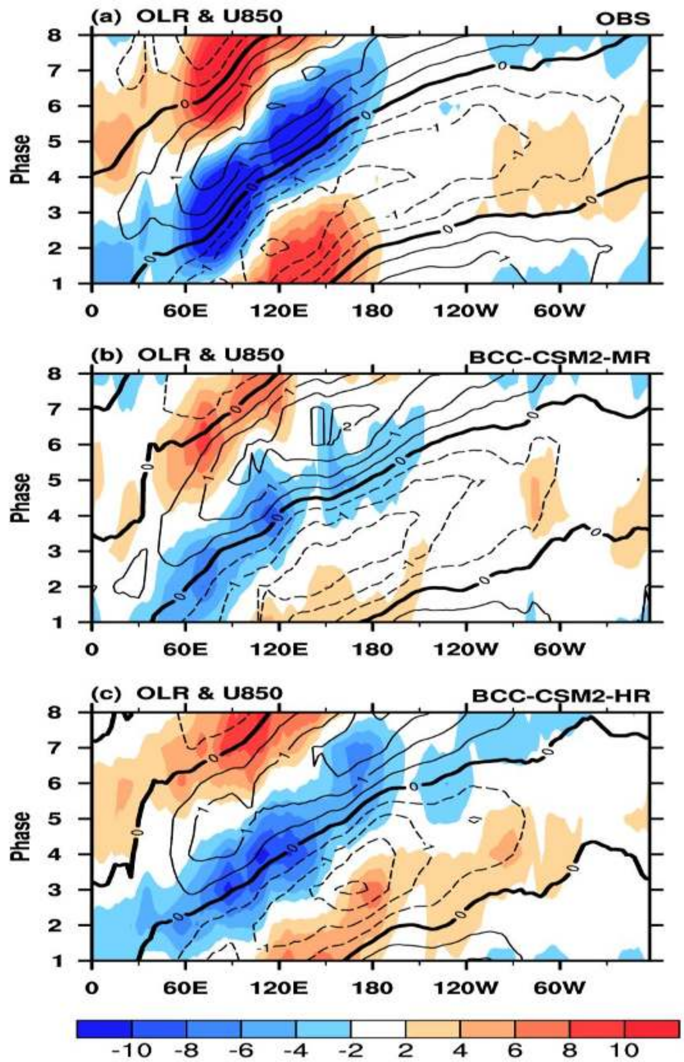

Figure 16. Hovmöller diagrams of MJO phase-composited OLR (shaded) and 850-hPa zonal wind anomalies (contour lines) averaged between 10°S and 10°N. The MJO phase is defined by the two principal components corresponding to leading multivariate EOFs of OLR, 850-hPa and 200-hPa zonal wind anomalies as in Wheeler and Hendon (2004).

https://doi.org/10.5194/gmd-2020-284
Preprint. Discussion started: 26 October 2020

Geoscientific Model Development
Discussions

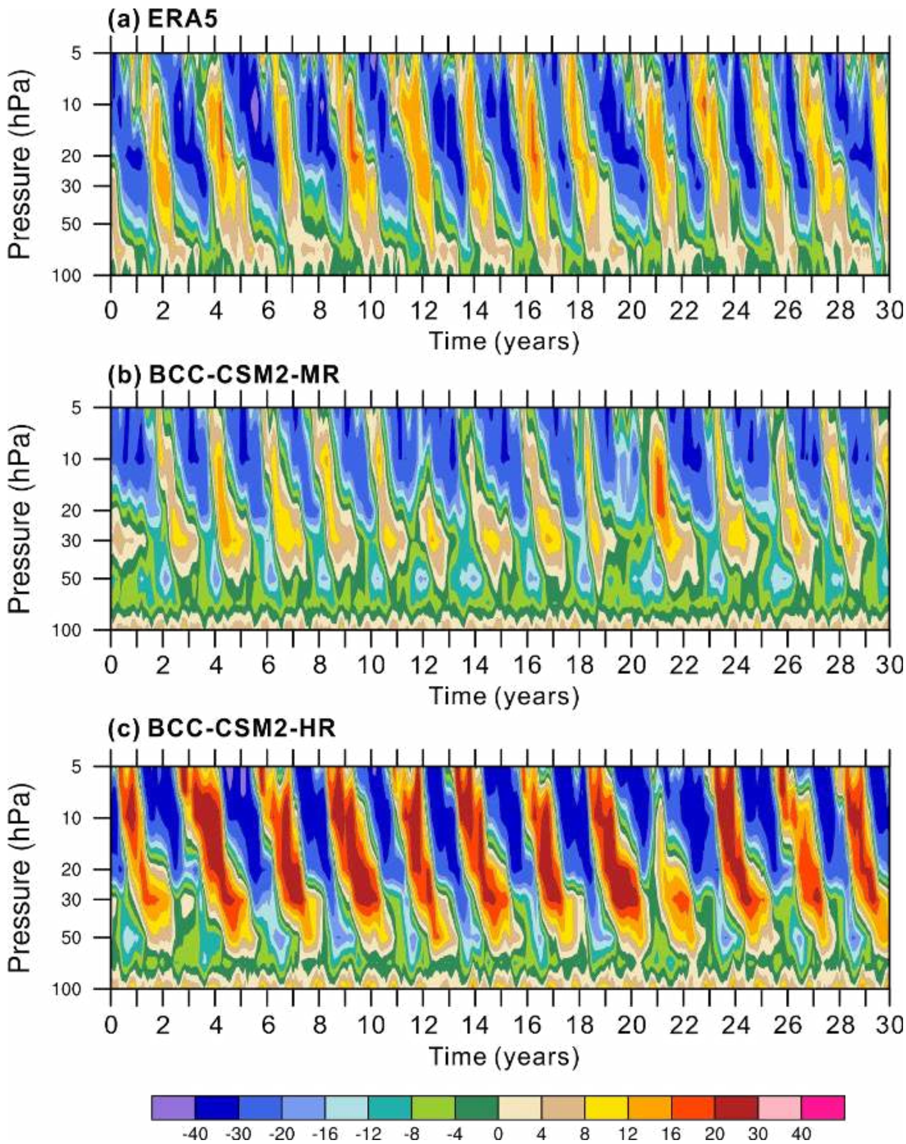

Figure 17. Tropical zonal winds ($m \cdot s^{-1}$) between 5°S and 5°N in the lower stratosphere for (a) ERA5 reanalysis (1981−2010), (b) BCC-CSM2-MR (1971−2000) and (c) BCC-CSM2-HR (1971−2000).

Geoscientific Model Development
Discussions

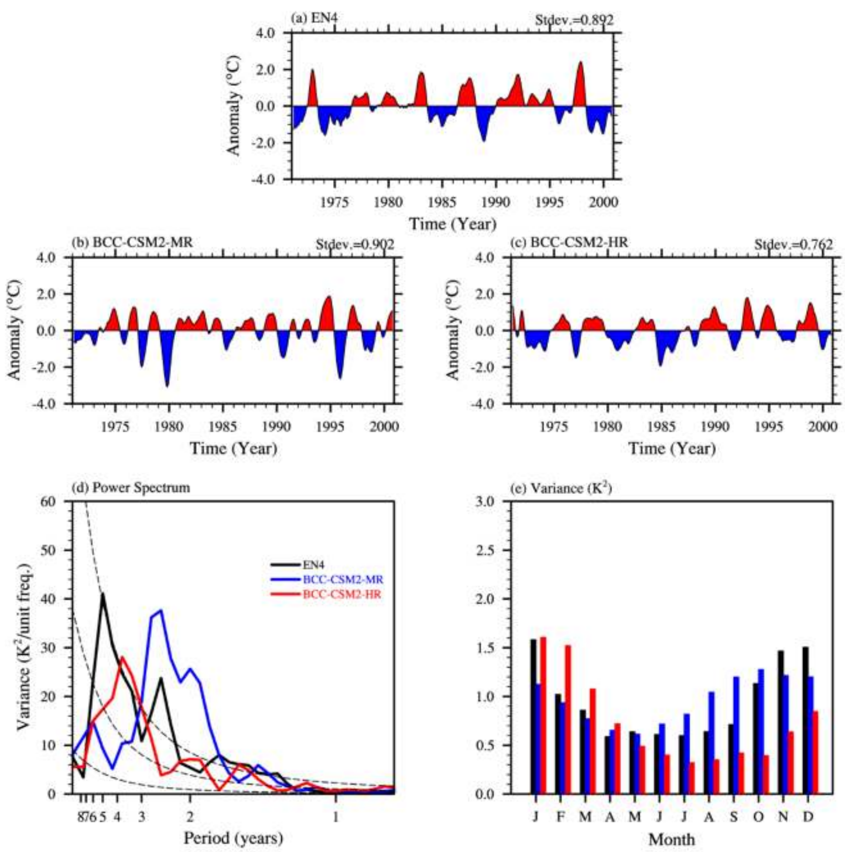

Figure 18. The time series of monthly Niño3.4 SST (5°N−5°S, 170°W−120°W) anomalies for (a) EN4 observation, (b) BCC-CSM2-MR, and (c) BCC-CSM2-HR during the period 1971-2000. (d) and (e) show their power spectrums and variances, respectively. The black, blue, and red solid lines in (d) and (e) show the results from EN4, BCC-CSM2-MR, and BCC-CSM2-HR.

https://doi.org/10.5194/gmd-2020-284
Preprint. Discussion started: 26 October 2020

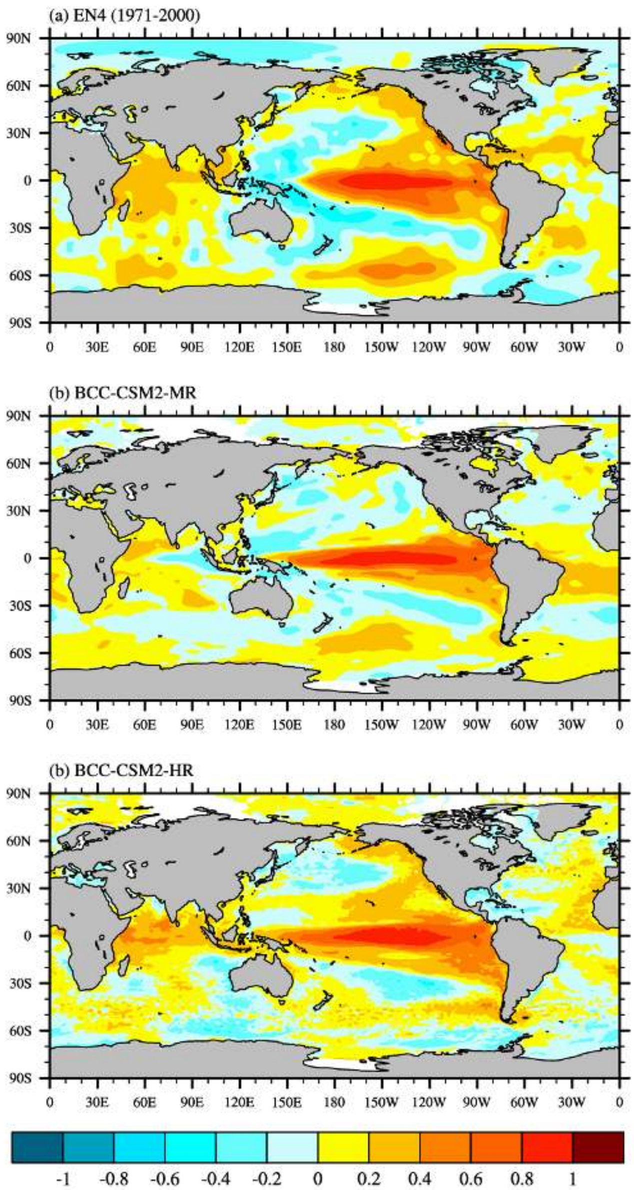

Figure 19. Correlation coefficients between SST and the Nino3.4 index from 1971 to 2000 for (a) EN4 data, (b) BCC-CSM2-MR, and (c) BCC-CSM2-HR. Contour intervals are 0.2.